TU DELFT

Kinetics of self-healing reaction in TBC with MoSi2 based sacrificial particles

Weichen (William) MAO
8/20/2013
MSc Materials Science and Engineering

Supervised by Dr. Ir. W. G. Sloof

Department of Materials Science and Engineering
Faculty of Mechanical, Maritime and Materials Engineering
Delft University of Technology

Abstract

The isothermal kinetics is investigated of a self-healing reaction in thermal barrier coatings (TBC) with $MoSi_2$ based sacrificial healing particles. Tablets cold pressed from yttria stabilized zirconia (YSZ) and $MoSi_2$ (with and without Boron) powder mixtures were annealed at 1100 and 1200 °C in open air. $MoSi_2$ is first oxidized to form amorphous SiO_2. Then, the amorphous SiO_2 wets the surface of YSZ particles. Finally, $ZrSiO_4$ is formed from the reaction between SiO_2 and YSZ. The amount of $ZrSiO_4$ and unreacted ZrO_2 after annealing was determined using X-ray diffraction (XRD), and is plotted against annealing time as a measure for the kinetics of this healing reaction. The reaction between SiO_2 and YSZ was finished within 5 hours at 1200 °C. Both of the reactants (i.e. YSZ and $MoSi_2$) are not fully consumed, and the amount of remnant ZrO_2 decreases with annealing temperature.

The kinetics of the zircon formation is dominated by the chemical reaction rather than the diffusion of the reacting species. This kinetics of zircon formation and ZrO_2 consumption can be described by a first-order reaction model and geometrical contraction model, respectively. The reaction rate at 1200 °C is about three times higher than that at 1100 °C. At 1100 °C the addition of Boron in the $MoSi_2$ particles effectively promotes the formation of amorphous SiO_2 and thereby accelerating the reaction rate by a factor of two. Particles of $MoSi_2$ with Boron are more promising as the healing agent in zirconia ceramics.

Table of Contents

1 Introduction

To meet the demand for higher efficiency of gas turbine engine, thereby saving fuel and reducing emission of CO_2, higher operating temperatures are desired. Then the materials of turbine blades, vanes and combustion chamber are required to withstand ever higher temperatures. Nowadays, the operating temperature in combustion chamber of engines is higher than the limit of Ni-based superalloy, advanced inner cooling technology as well as coatings are therefore applied. In a modern high temperature coating system as shown in Figure 1.1, an aluminide diffusion or MCrAlY overlay coating, often referred to as bond coat, is applied to the Ni-based superalloy substrate to provide protection against high temperature oxidation. A thermal barrier coating (TBC) which is commonly made of partially yttria stabilized zirconia (PYSZ) is applied to the bond coat as the top coating to further protect the blades against the high temperature environment. A thermally grown oxide (TGO) layer is formed between the BC and TBC during high temperature operation, which acts as a diffusion barrier for oxygen.

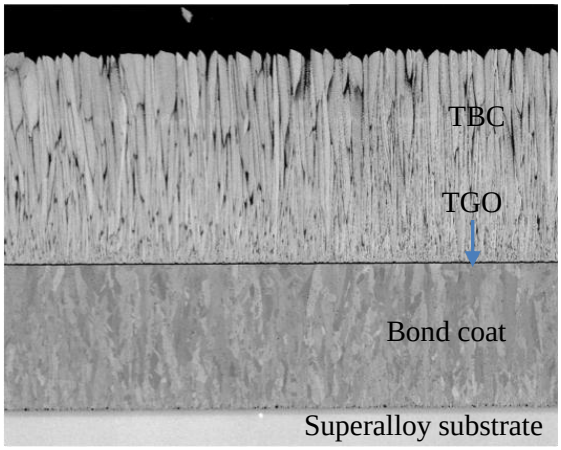

Figure 1.1: Modern high temperature coating system

However, due to the difference of thermal expansion between the TBC and the substrate, compressive stresses are developed in the TBC upon cooling from the operation temperature. Thus, small delamination cracks will be generated in TBC and TGO layer. These cracks may grow and ultimately coalescence into longer cracks. Cracks perpendicular to TGO layer are not detrimental, while cracks along the TGO will result in spallation of TBC. Such spallation of the TBC will reduce the lifetime of the coated components in turbine engines. Unlike BCs, current TBCs do not exhibit self-healing properties. So, to prolong the life span of TBCs, the study and development of self-healing TBC is attractive. A self-healing concept for TBCs was proposed by Sloof [1], in which $MoSi_2$ particles as healing agents encapsulated by an alumina scale are distributed at the bottom part of TBC. $MoSi_2$ is a stable compound at high temperature and not oxidized if fully covered by alumina outer scale. When cracks in the TBC propagate and break the alumina shell of the healing particles, $MoSi_2$ is exposed to the oxidizing environment. Then, SiO_2 is formed at high temperature that fills the cracks. Simultaneously, volatile MoO_3 is formed that may escape through the existing pores and cracks in TBC. Some preliminary experiments have been done, in which $MoSi_2$ particles and PYSZ powders are mixed and oxidized in air at 1200 °C. The results show that all the cavities and gaps in the mixture are fully filled by SiO_2, demonstrating that SiO_2 formed from $MoSi_2$ is capable to fill cracks in TBCs [2].

The chemical reaction between SiO_2 and YSZ to form $ZrSiO_4$ (zircon) is a vital step in the whole self-healing process. The final healing product $ZrSiO_4$ restores the mechanical integrity of TBC. Therefore, the isothermal kinetics of $ZrSiO_4$ formation from the reaction between YSZ and $MoSi_2$ is of great importance to the healing behaviour. Nevertheless, detailed kinetic study of this self-healing reaction has not yet been done. Therefore, the kinetics of $ZrSiO_4$ formation from the YSZ-$MoSi_2$ mixtures at high temperature is studied, and the mechanism of the reaction between SiO_2 and YSZ is discussed.

The thesis is structured as follows. Chapter 2 "Background" describes the fundamental knowledge that is necessary for the study on the kinetics of self-healing process in TBCs with $MoSi_2$ based sacrificial particles. A literature review on the kinetics of zircon formation from ZrO_2 and SiO_2 is also given. Chapter 3 "Experimental aspects" gives details about the sample preparation and oxidation and annealing experiments. The methods of investigation and the equipment used, are briefly explained. Chapter 4 "Results and discussion" describes and discusses all experimental results with a detailed analysis. This includes the kinetic behaviour of zircon formation and the reaction mechanism. The conclusion are presented in Chapter 5. Finally, some recommendations for further research are given in Chapter 6.

2 Background

2.1 Principle properties of $ZrSiO_4$, Yttria-stabilized ZrO_2 and SiO_2

Zircon (zirconium silicate) is one of the natural minerals that can be found in earth crust. Zircon is known as an oxide ceramic and refractory material that find its application as construction material or protective coating in glass and steel production industry due to its excellent thermal properties such as low thermal conductivity and low thermal expansion [3]. Zircon crystals have a body-centered tetragonal structure (space group $I4_1/amd$, Pearson symbol tI24) and consist of chains of alternating edge-linked oxygen tetrahedral and triangular dodecahedra with Si and Zr atoms at the center parallel to the c-direction, respectively. The chains are laterally connected through edge-sharing ZrO_8 dodecahedra[4], as shown in Figure 2.1. Since the cracks in YSZ will be healed by $ZrSiO_4$, the thermal conductivity and thermal expansion of $ZrSiO_4$ and ZrO_2 are compared in Table 2.1.

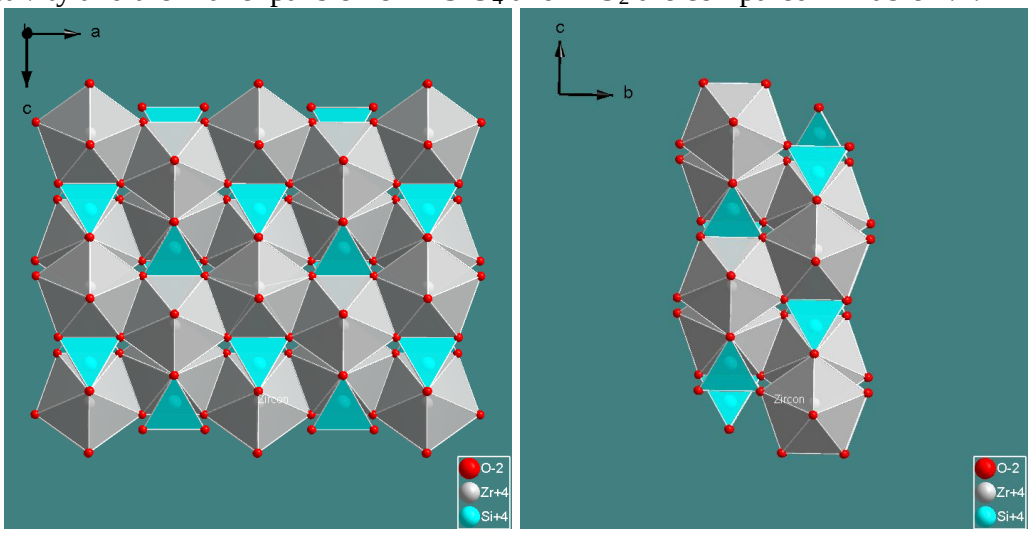

Figure 2.1: Crystal structure of zircon (ICSD 71945)

Table 2.1: Comparison of thermal properties between $ZrSiO_4$ and ZrO_2

	$ZrSiO_4$	YSZ (8 wt% Y_2O_3)	Baddeleyite[1]
Thermal expansion coefficient ($10^{-6}K^{-1}$)	4.2[3]	10.7[5]	7.56[6]
Thermal conductivity ($Wm^{-1}K^{-1}$)	2.6[6]	2.2[5]	

Zirconia (ZrO_2) is one of the most studied ceramic materials. Pure zirconia undergoes two phase transformations when cooling from high temperatures, namely: cubic to tetragonal at about 2340 °C and tetragonal to monoclinic at about 1170 °C. No high temperature phases can be retained by quenching to room temperature [7]. The transformation from the tetragonal crystal structure to the monoclinic crystal structure is accompanied by 8% volume expansion that leads ZrO_2 to crack upon cooling. Hence, for practical use, ZrO_2 is doped with oxides such that tetragonal and/or cubic phases can be stabilized at room temperature. Yttria (Y_2O_3) is often used as dopant for ZrO_2. Then, the cubic/tetragonal fluorite structure of ZrO_2 is retained with some of the Zr^{4+} ions in the ZrO_2 lattice replaced by Y^{3+} ions. Thus oxygen vacancies are generated which facilitates the diffusion of O^{2-} ions in stabilized ZrO_2. Scott [7] studied the phase relationships of the ZrO_2-Y_2O_3 system and proposed the phase diagram as shown in Figure 2.3. Different non-equilibrium ZrO_2 phases can be retained at room temperature depending on the amount of Y_2O_3 added. Metastable tetragonal structure can be

[1] Monoclinic phase of ZrO_2

obtained at room temperature with 3 to 6 mol% Y_2O_3 by quenching from the melting point. The phase composition of the ZrO_2 - Y_2O_3 mixture at room temperature depends on the heating temperature and holding time as well as the cooling rate. For example, ZrO_2 with 6-11 mol% $YO_{1.5}$, if holding time at 1200 °C is long enough, tetragonal and cubic phase are in equilibrium. The amount of Y_2O_3 in each phase can be determined from the solvus line in the phase diagram. After quenching to room temperature, monoclinic phase will be formed and both tetragonal and cubic phases are retained.

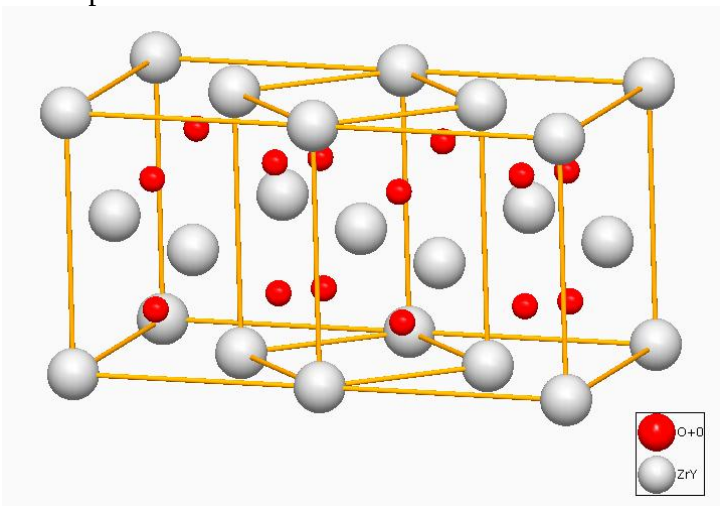

Figure 2.2: Defect fluorite structure of yttria-stabilized zirconia (Pearson database 1520514, occupation factor for O lattice site is 0.991)

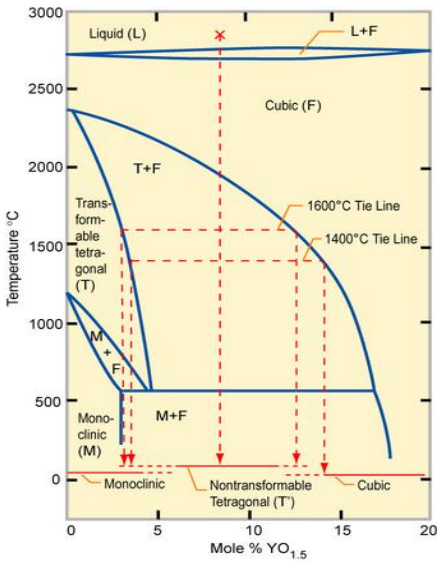

Figure 2.3: Phase diagram of the zirconia rich portion of ZrO_2-$YO_{1.5}$ system [3].

In addition to the amorphous structure, silica (SiO_2) has several different crystalline forms, such as: quartz, tridymite and cristobalite. All these crystalline forms are composed by the same basic unit of tetrahedral SiO_4 but in different arrangement. At room temperature rhombohedral α-quartz is the most stable phase, and it transforms to β-quartz (hexagonal) at 574 °C. At 870 °C it converts into tridymite. Cristobalite (cubic) is only stable at 1470 °C, but still can exist metastably at lower temperatures. Cupid and Seifert [8] studied the phase stabilities of the SiO_2-Y_2O_3 system and gave the calculated phase diagram as shown in Figure 2.4. It can be predicted that at around 1200 °C reaction between SiO_2 and Y_2O_3 may happen, thereby forming $Y_2Si_2O_7$.

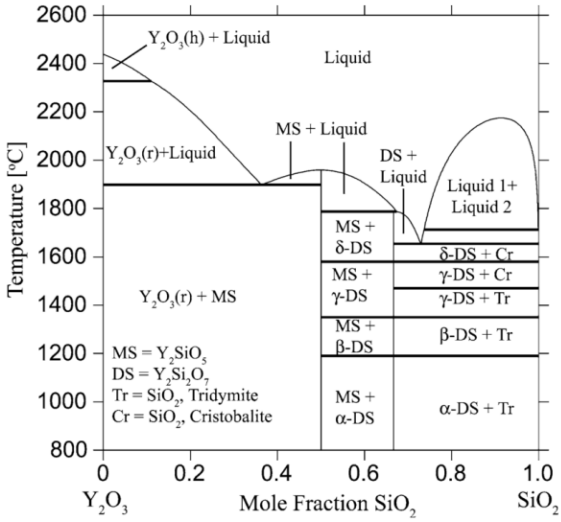

Figure 2.4: Calculated SiO_2-Y_2O_3 phase diagram, given in ref[4]

2.2 Oxidation behaviour of $MoSi_2$ powder

Numerous studies on the oxidation of $MoSi_2$ material in air has been reported before. The oxidation process of $MoSi_2$ is a relatively complex process. Starting from 500 °C $MoSi_2$ can be oxidized and both MoO_3 and SiO_2 are formed below 800 °C, expressed as

$$MoSi_2(s) + 3.5O_2(g) = MoO_3(s) + 2SiO_2(s) \qquad (<800\ °C)$$

Above 800 °C oxidation of $MoSi_2$ consists of two steps. $MoSi_2$ is first oxidized to Mo_5Si_3 whose reaction formula can be expressed as

$$5MoSi_2(s) + 7O_2(g) = Mo_5Si_3(s) + 7SiO_2(s) \qquad (>800\ °C)$$

Formation of Mo_5Si_3 is thermodynamically more favourable than the formation of MoO_3 directly from $MoSi_2$ when the temperature is above 800 °C [9]. Mo_5Si_3 can be further oxidized to form MoO_3 following the reaction formula

$$Mo_5Si_3(s) + 10.5O_2(g) = 5MoO_3(g) + 3SiO_2(s) \qquad (>800\ °C)$$

The melting point of MoO_3 is 801 °C, and the MoO_3 formed at high temperature will evaporate and condense on surfaces colder than 800 °C. The solid SiO_2 formed is reported to be in amorphous structure when oxidation is at 1100 °C [10]. The oxidation of $MoSi_2$ will be suppressed if a continuous SiO_2 passive scale is formed.

2.3 Volume effect of ZrO_2-SiO_2 reaction and $MoSi_2$ oxidation

Since ZrO_2, SiO_2 and $ZrSiO_4$ have different crystal structure, the molar volume of the three materials are different. As a result there is a volume change in the system after the reaction between ZrO_2 and SiO_2. The molar volume of a material can be calculated through equation:

$$V_m = \frac{N_A}{Z} V_{cell} \qquad (2.1)$$

, or

$$V_m = \frac{M}{\rho} \tag{2.2}$$

, where N_A is the Avogadro's constant, V_{cell} is the volume of one unit cell, Z is the number of molecules in each unit cell, M is molar mass and ρ is density. So the molar volume of tetragonal ZrO_2 can be calculated as 20.2 cm^3 (data selected from Pearson database 1520514, V_{cell} = 67.15 A^3, Z = 2). The molar volume of $ZrSiO_4$ is obtained as 40.2 cm^3 (ICSD 71945, V_{cell} = 267 A^3, Z = 4). The molar volume of amorphous SiO_2 is estimated as 28.9 cm^3 (ρ = 2.08 g/cm^3, M = 60.08 g/mol). Thus it is expected that there is a volume shrinkage of ZrO_2-SiO_2 reaction.

Similarly, the volume effect of the oxidation of $MoSi_2$ can also be predicted. Molar volume of $MoSi_2$ is calculated as 24.3 cm^3 (PDF 00-041-0612, V_{cell} = 80.57 A^3, Z = 2). Since the MoO_3 is volatile at temperature higher than 800 °C, the only oxidation product remaining in the system is SiO_2. Compared with the molar volume of amorphous SiO_2, a 138 % volume expansion of the oxidation of $MoSi_2$ is expected. The volume effect of the chemical reactions that take place in self-healing process is very important. The volume expansion of oxidation of healing particle $MoSi_2$ is necessary for crack healing, because cracks can only be filled with SiO_2 formed when the volume of oxidation product is larger than the original healing particles. The volume effect of ZrO_2-SiO_2 reaction is also beneficial for crack healing, since volume shrinkage of the formation of zircon will tend to close the crack gap.

2.4 Formation of zircon from ZrO_2 and SiO_2

Study of zircon formation from reaction between silica and zirconia dated back to several decades ago. The thermodynamics and kinetics of formation and decomposition of zircon have been investigated. Butterman and Foster [11] have proposed an early version of ZrO_2-SiO_2 quasi-binary phase diagram (see Figure 2.5), which shows that $ZrSiO_4$ is a stable phase until its decomposition temperature at about 1676 °C. No other compound will be formed by the reaction between ZrO_2 and SiO_2 below the decomposition temperature. Kaiser et al. [12] reviewed recently the thermal stability of zircon using the results published earlier. They studied the effects of particle size and impurity on the temperature of zircon formation and decomposition using high temperature X-ray diffraction. Their experimental results showed, that $ZrSiO_4$ powder can decompose as low as 1450 °C when the material is not 100 % pure. The formation of zircon from stoichiometric blends of ZrO_2 (stabilized) and SiO_2 (fused silica and cristobalite) powders was also studied and it was shown that $ZrSiO_4$ forms rapidly above 1300 °C and decompose above 1500 °C into tetragonal ZrO_2 and amorphous SiO_2; see Figure 2.6. Unstabilized zirconia can react to form zircon at 1200 °C after four hours while for yttria-stabilized zirconia zircon can only be observed above 1300 °C. However, this is not consistent with experimental result from Du et al. [13]. According to their XRD analysis, large amount of zircon is formed from silica and yttria-stabilized zirconia at temperatures as low as 1100 °C. However, it seems that the type of silica (fumed silica or cristobalite) has no effect on the zircon formation starting temperature [12].

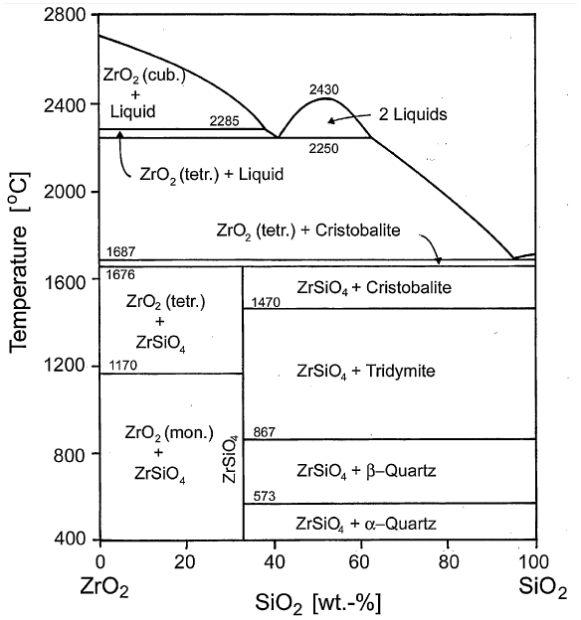

Figure 2.5: ZrO_2-SiO_2 phase diagram after Butterman and Foster

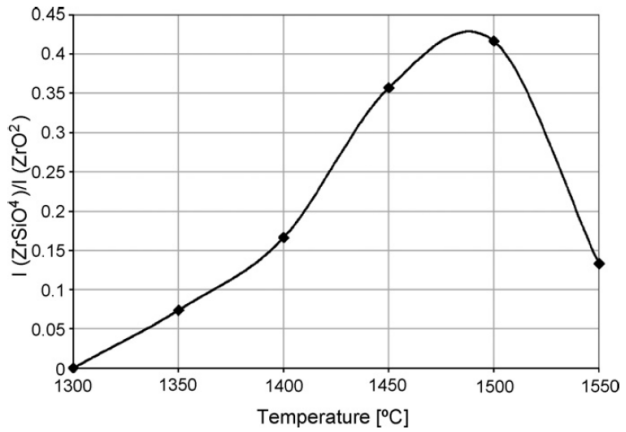

Figure 2.6: Formation of zircon from fumed silica-stabilized zirconia with heating rate 1K/min

The kinetics of isothermal zircon formation from ZrO_2 and SiO_2 between 1200 to 1400 °C has been investigated by many researchers [14-17]. It has been found that there is a large difference in the reaction rate between amorphous and crystalline SiO_2. The formation rate of zircon from equimolar mixtures of amorphous silica and amorphous zirconia at 1300 °C is studied by Itoh [14]. The kinetic curve is shown in Figure 2.7. It can be observed that formation of zircon starts rapidly after about 10 minutes and after about 30 minutes about 80 % is completed. Next, the yield rate of $ZrSiO_4$ becomes practically zero. Itoh suggested that the reaction between amorphous silica and zirconia predominate the transformation of amorphous silica to cristobalite at 1300 °C. The transformation of amorphous SiO_2 into crystalline SiO_2 is not detected during the zircon formation period (see Figure 2.7). Then, it is that zircon is formed exclusively by the reaction between amorphous SiO_2 and tetragonal ZrO_2. Similar S-shaped yield rate curves are reported by Mori et al. [15]. and Spearing [16] who synthesized zircon via milled SiO_2 and ZrO_2. It was proposed that the reaction mechanism is the same within the temperature range of 1200 to 1400 °C. The reaction rate increases with temperature, as shown in Figure 2.8.

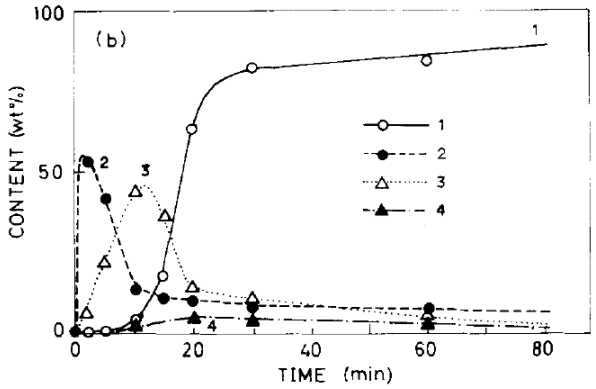

Figure 2.7: Fraction of species in mixture of ZrO_2 and SiO_2 heated at 1300 °C as a function of time: (1) $ZrSiO_4$; (2) t-ZrO_2; (3) m-ZrO_2; (4) cristobolite. Data were obtained from XRD analysis of quenched samples[14]

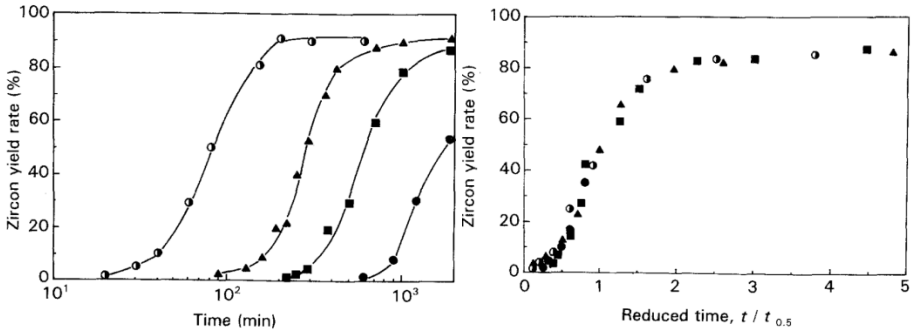

Figure 2.8: Zircon yield rate curve as function of time (left) and reduced time (right) at: 1200 °C, 1250°C, 1300°C, 1400°C[15]

Ramani et al. [18] investigated the kinetics of zircon synthesis from crystalline SiO_2 (quartz and cristobalite) at temperature range from 1250 to 1400 °C. It is found that quartz does not react with zirconia to form zircon in this temperature range. Cristobalite reacts with ZrO_2 only above 1350 °C, but with a very low reaction rate. However, an amorphous transitional phase of SiO_2 is formed during the quartz-cristobalite transformation, and zircon is primarily formed from the reaction between ZrO_2 and this transitional phase. The fact that cristobalite reacts much slower than amorphous SiO_2 is also reported in the study of Kaiser et al. [12].

A mechanism for zircon formation from zirconia and silica have been proposed by Eppler [19, 20] and Veytizou et al. [17]. It is suggested that Si^{4+} are the only mobile cation species and diffuse through the zircon layer to react with ZrO_2 at the zircon-unreacted ZrO_2 interface. Marker experiment was performed by Eppler to prove this mechanism; see Figure 2.9. Pt wires which are inert to the reaction are used as markers and placed between ZrO_2 and SiO_2 layer before reaction. The reaction product was found to be confined at the ZrO_2 side. It was also observed that the square of the thickness of the product layer varies linearly with time, which indicates that diffusion of species are the rate-limiting step; see Figure 2.10. Veytizou et al. further illustrate the mechanism with hypotheses that the zircon product layer is non-stoichiometric and contains Si^{4+} interstitials and O^{2-} vacancies. SiO_2 first dissociate into Si^{4+} interstitials and Si vacancies. Then the Si^{4+} moves through zircon layer via interstitial sites and dissolves into the tetragonal ZrO_2 crystallites. The oxygen vacancies move in the opposite direction, from ZrO_2 across the zircon product layer into SiO_2; see Figure 2.11. The zircon phase starts to precipitate at the interface between ZrO_2 and zircon layers when the solubility limit of silicon in ZrO_2 crystal is reached.

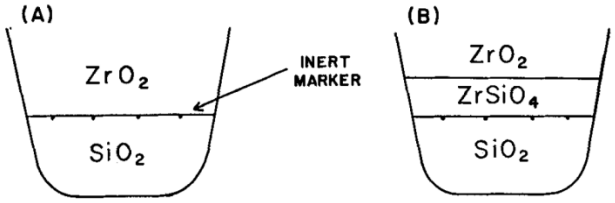

Figure 2.9: Schematic of marker experiment, performed by Eppler [20]

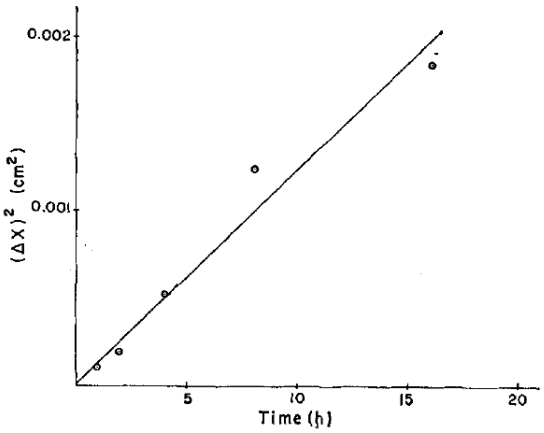

Figure 2.10: Thickness of zircon layer as a function of time [20]

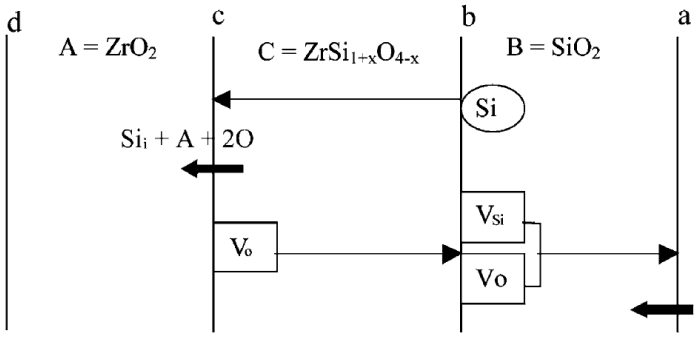

Figure 2.11: Reaction mechanism in one-dimensional framework [17]

In summary, a detailed study on thermodynamics and kinetics of zircon formation from yttria-stabilized zirconia and silica is lacking. A ternary phase diagram of ZrO_2-SiO_2-Y_2O_3 system is not available yet. A discrepancy exists about the temperature at which zircon starts to form from zirconia doped with yttria. Whether or not the YSZ-SiO_2 reaction can take place below 1200 °C is uncertain. Probably the starting temperature for zircon formation depends on the condition of raw materials, and no research has been done on zircon formation from YSZ-$MoSi_2$ mixture. A full quantitative description of the reaction kinetics of zirconia and silica to form zircon, including the activation energy, is not available yet. Although mechanism of reaction between ZrO_2 and SiO_2 has already been proposed, the experimental proof of such mechanism is not completed yet. Experiments such as determining the over-stoichiometry and element concentration profile across both the zircon and ZrO_2 layer are not reported yet. Moreover, explanation is also not given yet for the large difference in the reaction rate between crystalline and amorphous SiO_2 with ZrO_2.

2.5 Kinetic study of solid-state reaction through thermal analysis

The rate of a solid-state reaction at a constant temperature can be expressed as:

$$\frac{d\alpha}{dt} = kf(\alpha) \tag{2.3}$$

, or its integral form:

$$g(\alpha) = kt \tag{2.4}$$

, where $f(\alpha)$ and $g(\alpha)$ are known as the conversion functions or rate expressions and α is the conversion fraction, defined by:

$$\alpha = \frac{m_0 - m_t}{m_0 - m_\infty} \tag{2.5}$$

Here, m_0 is initial weight, m_t is weight at time t, and m_∞ is final weight. Since a thermally activated process is considered, the Arrhenius relation is usually adopted for the rate coefficient k, hence:

$$k = A\exp(-E/RT) \tag{2.6}$$

, in which A is the pre-exponential or frequency factor and E is the activation energy.

The conversion functions, $f(\alpha)$ and $g(\alpha)$, are derived based on a model adopted to describe the reaction mechanism. Generally, the reaction models are divided into nucleation, geometrical contraction, diffusion and reaction-order. Each model has its own unique form of the conversion function; see Table 2.2. By fitting the experimental data, in terms of conversion fraction versus reaction time, to the conversion functions, may hint to the mechanism of a specific solid-state reaction. However, to obtain a full kinetic description of a reaction, also the rate coefficient (i.e. the activation energy together with the frequency factor) must be determined.

Table 2.2: Conversion functions for different models; Khawam and Flanagan [21].

model		$g(\alpha) = kt$
Nucleation models	Power law	$\alpha^{1/n}$
	Avrami-Erofeev (An)	$[-\ln(1-\alpha)]^{1/n}$
	Prout-Tompkins (B1)	$\ln[\alpha/(1-\alpha)] + c^a$
Geometrical contraction models	Contracting area (R2)	$1-(1-\alpha)^{1/2}$
	Contracting volume (R3)	$1-(1-\alpha)^{1/3}$
Diffusion models	1-D diffusion	α^2
	2-D diffusion	$[(1-\alpha)\ln(1-\alpha)] + \alpha$
	3-D diffusion	$[1-(1-\alpha)^{1/3}]^2$
	Ginstling-Brounshtein	$1-(2/3)\alpha-(1-\alpha)^{2/3}$

Reaction-order models	Zero order	α
	First order	$-\ln(1-\alpha)$
	Second order	$[1/(1-\alpha)]-1$
	Third order	$(1/2)[(1-\alpha)^{-2}-1]$

The conventional method to determine the rate constant through isothermal analysis (from series of conversion data as a function of time at different but constant temperatures) may be time consuming. Alternatively, the parameters for the rate constant (i.e. the activation energy together with the frequency factor) may be obtained from non-isothermal calorimetric experiments, such as: differential scanning calorimetry (DSC) or differential thermal analysis (DTA). Take DTA for example, the difference in temperature between the sample and reference material is recorded while both are under the same heating programme. When a thermal event such as chemical reaction occurs, the sample temperature will deviate much from reference material temperature and thus a peak will show in the curve, as shown schematically in Figure 2.12.

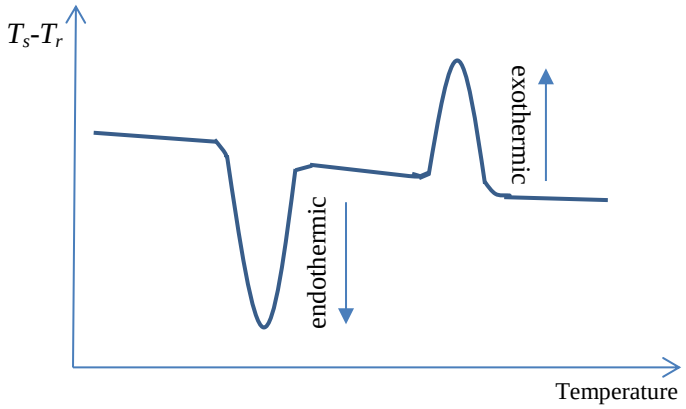

Figure 2.12: Schematic picture of a typical DTA curve

Kissinger [22] proposed a relation between the peak temperature in the DTA/DSC curve, heating rate and the activation energy of the thermal event that corresponds to the peak. By combining Equation (2.3), (2.6) and the conversion function for reaction-order models, the following equation can be obtained:

$$\frac{d\alpha}{dt} = A\exp(-\frac{E_a}{RT})\times(1-\alpha)^n \qquad (2.7)$$

When the maximum of reaction rate is reached, it holds that:

$$\frac{d}{dt}(\frac{d\alpha}{dt}) = 0 \qquad (2.8)$$

Since both the temperature T and the conversion fraction α is a function of time, on differentiating (2.7) the result is:

$$\frac{d}{dt}(\frac{d\alpha}{dt}) = A\exp(-\frac{E_a}{RT})(1-\alpha)^n\left[\frac{E_a}{RT^2}\frac{dT}{dt} - n(1-\alpha)^{-1}(\frac{d\alpha}{dt})\right] \qquad (2.9)$$

Thus, from (2.8) and (2.9) it is obtained that:

$$\frac{E}{RT^2}\frac{dT}{dt} = nA(1-\alpha)^{n-1}\exp(-\frac{E_a}{RT}) \tag{2.10}$$

By assuming that the reaction rate reaches maximum at the temperature where the DSC/DTA curves show a peak T_p, the following relation can be written:

$$\ln(\frac{\beta}{T_p^{\,2}}) = -\frac{E_a}{RT_p} + \ln(\frac{nAR}{E_a}) + (n-1)\ln(1-\alpha) \tag{2.11}$$

, or be expressed in differential form as:

$$\frac{d(\ln\frac{\beta}{T_P^{\,2}})}{d(\frac{1}{T_P})} = -\frac{E_a}{R} \tag{2.12}$$

, where β is the heating rate (dT/dt), R is gas constant, and E_a is the activation energy. Thus, by plotting $\ln(\beta/T_p^2)$ against $1/T_p$ for a series of experiment data, then the slope of a straight line through the experimental data corresponds to E_a/R. Similarly, based on the assumption that the degree of reaction at the peak temperature of DSC/DTA curve is a constant value and independent of heating rate, Ozawa [23] reached another equation, namely:

$$\log(\beta) = const - \frac{0.4567E_a}{RT_p} \tag{2.13}$$

Then from a plot of $\log(\beta)$ versus $1/T_p$, the activation energy E_a can also be obtained. Both the Kissinger and Ozawa treatment are valid under the condition that the reaction rate at a constant degree of reaction α is a function of temperature only [24], and that one reaction mechanism occurs in the temperature range considered.

2.6 One-dimensional diffusion controlled reaction kinetics

In many cases the overall rate of a solid-state chemical reaction process is determined by the transportation of a reactant. In these diffusion controlled reactions the product is generated at contact region between two reactants, and this product remains there if it is immobile [25]. As a result, the two reacting solids are in separate crystal lattices with the product layer as a barrier in between the reactants. If the reaction is to continue, one reactant species must diffuse across the barrier of product whose thickness increases as reaction proceeds. The one-dimensional model of such reaction mechanism is depicted in Figure 2.13, in which A and B represents two different reactants, AB is reaction product, x is the distance from AB/B interface into AB, l is the thickness of product layer.

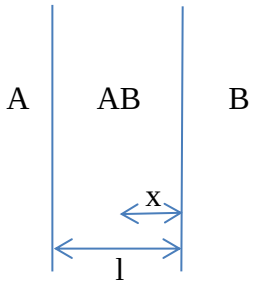

Figure 2.13: Schematic one-dimensional diffusion through a flat plane

If the rate of chemical reaction between A and B is sufficiently fast, the rate of total reaction process will mainly depend on the diffusion of species across the product layer. The formation of AB decreases with the increase of the thickness of AB layer. According to Fick's first law, the rate of increase of AB layer thickness can be expressed as:

$$\frac{dl}{dt} = -D\frac{M_{AB}}{M_B\rho}\left.\frac{dC}{dx}\right|_{x=l} \tag{2.14}$$

where M_{AB} and M_B are the molar weights of AB and B respectively, D is the diffusion coefficient, ρ is the density of product AB and C is the concentration of B in AB. Assuming that the concentration profile of B in AB is linear, then:

$$\left.\frac{dC}{dx}\right|_{x=l} = -\frac{C_2 - C_1}{l} \tag{2.15}$$

In which C_2 and C_1 are the concentration of reactant B at AB/B and AB/A interface respectively. Thus combining these two formula it is obtained:

$$\frac{dl}{dt} = D\frac{M_{AB}}{M_B\rho}\frac{(C_2 - C_1)}{l} \tag{2.16}$$

Integration of Equation (2.16) gives:

$$l^2 = 2D\frac{M_{AB}(C_2 - C_1)}{M_B\rho}t \tag{2.17}$$

$$l^2 = kt \tag{2.18}$$

Equation (2.18) is known as the parabolic growth rate law, which describes the reaction kinetics in case of an infinite flat plane without considering a shape factor. Therefore, such parabolic growth rate law can often be used to explain the growth of oxides scale formed at metal surfaces. Since the thickness of the product layer is linearly proportional to the conversion fraction α, Equation (2.18) can also be expressed as:

$$\alpha^2 = k't \tag{2.19}$$

, which is exactly the same as the conversion function for 1-D diffusion model given in Table 2.2.

It is worth noting that the parabolic growth rate law is only valid when [26]:

1. Transportation of ions across the layer of reaction product is the rate-controlling process.
2. The product layer is a compact and adherent, i.e. short-circuit diffusion such as diffusion along grain boundaries can be neglected.
3. Thermodynamic equilibrium is established at both product-reactant interfaces, i.e. the concentration of certain species at interface remains constant.

2.7 Reaction kinetics of the contracting sphere model

When a solid particle has spherical shape and the reaction occurs homogeneously at the particle surface, the reaction front will progress towards the centre of the particle, then following equation holds:

$$r = r_0 - k_G t \tag{2.20}$$

, where r is the radius at time t, r_0 is the original particle radius, and k_G is the reaction rate constant that describes the progressing speed of the reaction interface. The unreacted volume of the particle is

$$volume = \frac{4}{3}\pi r^3 \tag{2.21}$$

Therefore, the conversion fraction α can be expressed as

$$\alpha = \frac{\frac{4}{3}\pi r_0^{\,3} - \frac{4}{3}\pi r^3}{\frac{4}{3}\pi r_0^{\,3}} = 1 - \frac{r^3}{r_0^{\,3}} \tag{2.22}$$

Substitution into Equation (2.20), it follows that:

$$1-(1-\alpha)^{1/3} = \frac{k_G}{r_0} t \tag{2.23}$$

, which is the conversion function R3 of the geometrical contraction model.

Equation (2.23) can be applied under the condition that the diffusion of reacting species across the product layer is much faster than the rate of the chemical reaction that occur at the spherical particle interface.

3 Experimental aspects

3.1 Sample preparation

The raw powders of SiO_2, $MoSi_2$ and yttria stabilized ZrO_2 used in this study, are listed in Table 3.1.

Table 3.1 Materials and brand name

Materials	Brand
Yttria-stabilized ZrO_2 (YSZ)	Sulzer NS204, 8 wt% Y_2O_3
$MoSi_2$ with 2 wt% Boron	ChemPur
$MoSi_2$	ChemPur
Quartz SiO_2	Sigma Aldrich
Amorphous SiO_2	ABC Nanotech

Four different powder mixtures with YSZ were prepared, namely: with the two types of $MoSi_2$ powder (with and without the addition of Boron) and with the two types of SiO_2 powder (quartz and amorphous SiO_2). In each mixture, the molar ratio of element Zr over Si equals to one. Before mixing the powders, both two types of $MoSi_2$ powder were dried in autoclave (TAMSON) at 80 °C for 1 hour to prevent agglomeration of particles. A homogeneous powder mixture was obtained by using a polyethylene bottle (250 ml) filled with 15 g powder putting in a tubular mixer (Turbula T2c) for 3 hours. Next, the powder mixture was cold pressed into circular tablets using a 12 mm-diameter die and a uniaxial pressing machine (Carver M3853). In order to dense tablets, the load was slowly applied until it reached 9500 pounds (4.3 tons) and then kept for 5 minutes at this pressure. The mass of each tablet prepared from YSZ-$MoSi_2$-B and YSZ-$MoSi_2$ mixture was 0.8 and 0.9 g, respectively, corresponding with a height of about 1.9 and 2.2 mm. The mass of a YSZ-SiO_2 tablet is about 0.7 g corresponding with a height of about 2.7 mm.

To enhance the integrity of the tables, 4 wt% polyvinyl alchol (PVA) solution was applied as a binder. The PVA solution was added only to the YSZ-SiO_2 powder mixture.

3.2 Isothermal annealing experiments

Annealing of the green-body tablets at 1100 and 1200 °C, was executed in a horizontal tube furnace (Lenton LTF 14/25/180) with an 25 mm inner diameter alumina tube open to air. The tablets were placed in a boat-shape alumina crucible (DEGUSSIT AL23, FRIATEC). After the target temperature inside the furnace reached stably, the crucible with tablet was slided directly into the center furnace hot-zone with an Inconel rod. After annealing the crucible with the sample was removed quickly from the furnace hot-zone and cooled down instantly in ambient air. No breakage of tablets due to instantly heating and cooling was observed.

3.3 Methods of Investigation

3.3.1 Particle size analysis

The particle size distribution of raw powders is measured by a laser diffraction method. When a laser beam with fixed wavelength passes through a dispersed powder sample, the beam light

will be scattered by the particles at a wide range of angles that directly relate to particle size. Large particles scatter light at small angles relative to the incident beam whereas large angle scattering occurs at small particle size. Moreover, the intensity of scattered light increases with particle size. Thus, by placing a series of detectors at fixed position over a wide range of angles, the angular variation in the intensity of scattered light can then be obtained. Using the Mie theory [27], the size distribution of powder sample can be determined. The size of a particle is expressed as the diameter of a volume equivalent sphere. The equipment used in this study is the Mastersizer X, Malvern Instruments, UK.

3.3.2 X-ray diffractometry

X-ray diffraction (XRD) is a common characterization method used to identify the phases of materials [28]. A diffractogram was recorded in the 2θ–range from 15° to 90° using Cu Kα radiation of the green sample and after each annealing period. In this study XRD analysis was also a tool to determine quantitatively the reaction kinetics. The rate of the reaction between ZrO_2 and SiO_2 can be derived from the rate of ZrO_2 consumption. To this end, the decrease of the intensity of ZrO_2 peaks was measured after different annealing times. Similarly, the rate of $ZrSiO_4$ formation was determined from the measured increase of the $ZrSiO_4$ peak intensity. Here, all the ZrO_2 peaks within the 2θ–range from 48° to 52°, which includes both monoclinic and tetragonal ZrO_2 phase, were selected to quantify the amount of ZrO_2. The $ZrSiO_4$-(200) reflection in the 2θ-range from 26° to 31° is selected to determine the $ZrSiO_4$ formation.

The XRD measurements were performed with a Bruker D5005 diffractometer equipped with Huber incident-beam monochromator and Braun PSD detector (Cu Kα1). The details of XRD measurements of three diffractograms recorded are listed in Table 3.2. The parameters for recording all diffractograms were kept the same.

Table 3.2: Parameters of XRD scans

Parameters	diffractogram 1	diffractogram 2	diffractogram 3
2θ range	15°-90°	48°-52°	26°-31°
Divergence Slit	1G16	1G16	1G16
Slit width	Not applied	Not applied	Not applied
Scatter screen height	5mm	5mm	5mm
Sample holder	SP52	SP52	SP52
Step size	0.0387°	0.0387°	0.0387°
Time/step	0.5s	5s	5s
Rotation speed of sample	30 rpm	30 rpm	30 rpm

As an illustration of the quantitative analysis, the diffractograms including the selected ZrO_2 and $ZrSiO_4$ XRD lines are shown in Figures 3.1 and 3.2, respectively. The change in peak area after annealing is evident. The net integrated intensity in the 2θ–range from 48° to 52° is taken as a measure for the ZrO_2 amount in the sample. It is assumed that throughout the whole annealing process no texture was developed in the sample. Thus, by calculating the ratio between the net integrated intensity before and after annealing, the fraction of unreacted ZrO_2 is obtained. The net integrated area of the $ZrSiO_4$ (200) peak is taken as the amount of $ZrSiO_4$ formed. Note that the net integrated intensities were determined using the "integrate" function embedded in "Origin Pro 8" software.

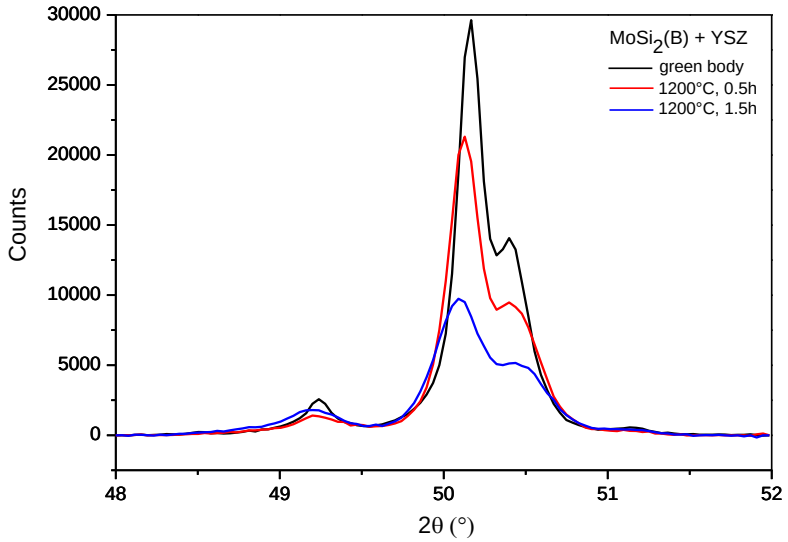

Figure 3.1: XRD pattern of ZrO_2 peaks before and after annealing

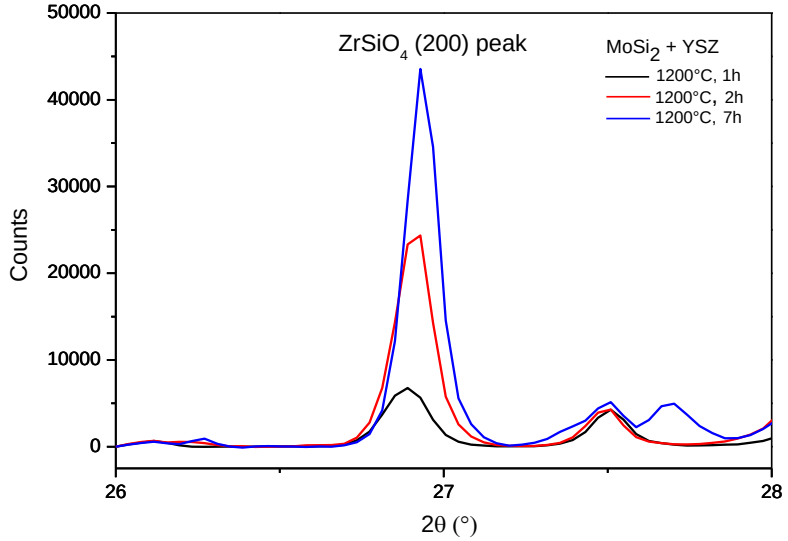

Figure 3.2: XRD pattern of $ZrSiO_4$ (200) peak after different annealing time

After annealing for 3 hours, several diffraction lines of unidentified phases were observed in 2θ-range from 48° to 52° and overlap with the ZrO_2 peaks. These lines give rise to the peak area of ZrO_2 , but were eliminated by curve fitting of the peaks in the diffractogram (using "TopasP3" software).

3.3.3 Scanning electron microscopy (SEM) and X-ray microanalysis (XMA)

The morphology and chemical composition of samples was studied with scanning electron microscopy (SEM) [29], using a field-emission gun scanning electron beam microscope (JEOL JSM 6500F), equipped with an energy dispersive spectrometer (EDS, Thermoscientific Ultra dry detector operated with Noran System 7 acquisition software) for X-ray microanalysis (XMA) [29]. The basic principle of SEM is schematically shown in Figure 3.3. A focused primary electron beam interacts with sample and generates different signals that may be used for investigation, such as: backscattered electrons, secondary electrons and characteristic X-rays. The backscattered electrons are primary electrons that deflect after elastic collision with atoms in the sample. The number of collision sites increases with the

number of electrons in an atom. Thus, the yield of backscattered electrons increases with the atomic number (Z). The inelastic collision between primary electrons and sample can ionize a number of sample atoms, and thus secondary electrons are generated. The energy of secondary electrons (0-50 eV) is usually much lower than that of the backscattered electrons. So, only secondary electrons from the region close to sample surface can escape and be detected. The secondary electrons give more information about the topography of sample surface, whereas the backscattered electrons reflect the element distribution in the sample. The characteristic X-rays are generated from the relaxation of ionized atoms and are able to offer quantitative information about chemical composition of materials.

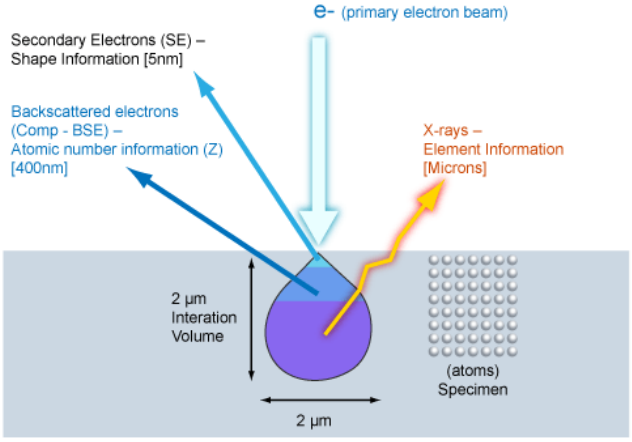

Figure 3.3: Schematic picture of interaction between primary electron beam and sample

To obtain a more accurate result for the local composition profile, electron probe microanalysis (EPMA) [30] was applied. A qualitative line profile was measured with the JEOL JXA-8900R microprobe employing wave dispersive spectroscopy (WDS) of the elemental X-ray lines of Zr-Lα and Si-Kα. For those spectral features the analysing crystals PETJ and TAP were selected, respectively. The electron beam energy used was 5 keV with a beam current of 20 nA. Measurement time for each spot is 5 seconds.

The annealed tablets used for SEM cross-section observation were first cut in half with precision diamond saw (IsoMet low speed saw, Buehler). The half-circular tablets were clamped between two pieces of iron plates with two screws to adjust tightness. Then, the cross-section surface was grinded with emery paper starting with 220 grit and finally with 2500 grit. Thereafter, the surface of the cross-sections was polished with 3 µm diamond grains on a soft cloth. Then, the sample was ultrasonic cleaned subsequently in acetone and iso-propanol and dried in an autoclave at 80 °C for 2 hours to evaporate remnant liquid in the pores of the sample. Prior to the SEM observations, the sample surface was coated (JEOL JEC-530 auto carbon coater) with a carbon layer of about 17 nm thickness to enhance the electric conductivity.

3.3.4 Thermal analysis

Differential thermal analysis (DTA) was applied to both $MoSi_2$ and $MoSi_2B$ powders and both YSZ-$MoSi_2$ and YSZ-$MoSi_2B$ powder mixtures to study the thermal behaviour during the annealing process. To this end, a SETERAM SETSYS Evolution 1750 in DTA-TG configuration (tube diameter of 15 mm) was used, with its schematics shown in Figure 3.4. The mass of each sample is about 20 mg. Reference material is an empty alumina crucible. All the samples were heated from room temperature to 1450 °C with a constant heating rate,

and subsequently cooled down to room temperature with cooling rate of 15 °C/min.. A flow of 50 ml/min. 'synthetic air' was applied. This gas is composed of dry pure N_2 and O_2 (both better than 5N) with a volume ratio of 4 to 1. Simultaneously, the mass change of the sample during the DTA experiment was recorded, which may offer additional information about the occurring chemical reaction. To determine the activation energy of the oxidation reactions, DTA experiments with different heating rates were executed, namely 2, 5, 10 and 20 °C/min.

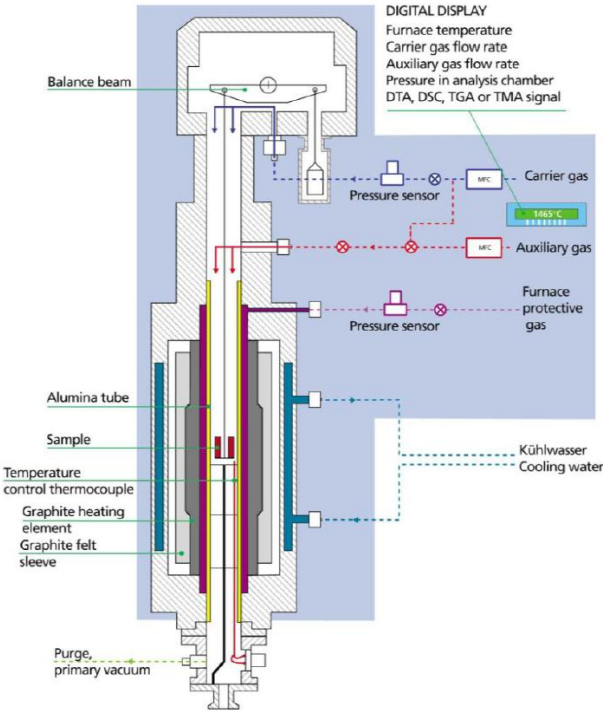

Figure 3.4: Schematic picture of the Setsys Evolution thermal analysis equipment

4 Results and discussion

4.1 Characterization of raw materials

The powders used as reactants to study the formation kinetics of zircon (cf. Table 3.1) were first characterized in terms of phase composition and morphology. XRD measurements, SEM observation and particle size analysis were applied on each type of powders (cf. Section 3.3). The YSZ powder used in the study is the same as used to deposit TBC's in jet engines. This YSZ powder is not fully stabilized, and is composed by both tetragonal (major phase) and monoclinic ZrO_2, as shown in Figure 4.1. SEM images show that most of the YSZ particles have a spherical shape. The particle size analysis shows that the average diameter of YSZ powder ranges from 20 to 80 µm with an average diameter of about 50 µm.

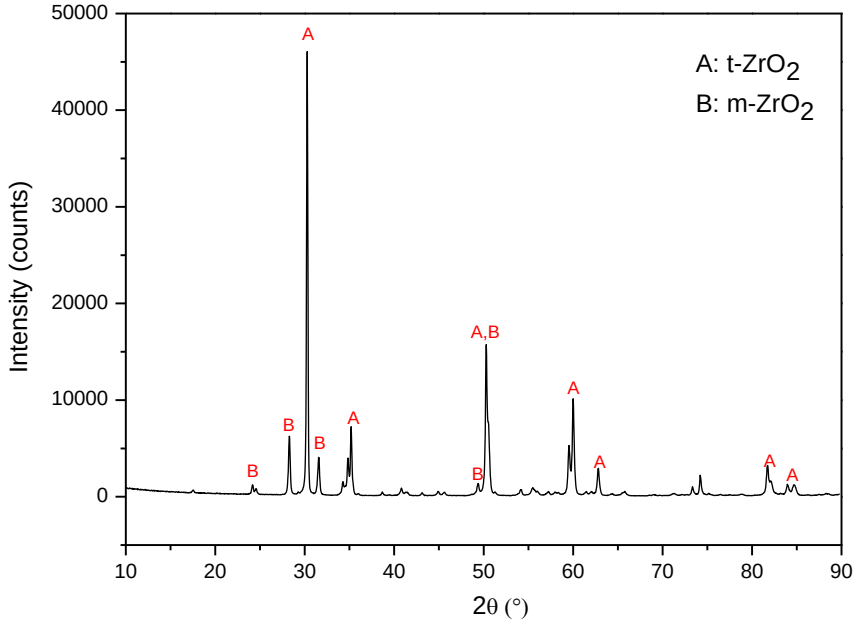

Figure 4.1: XRD pattern of YSZ powder

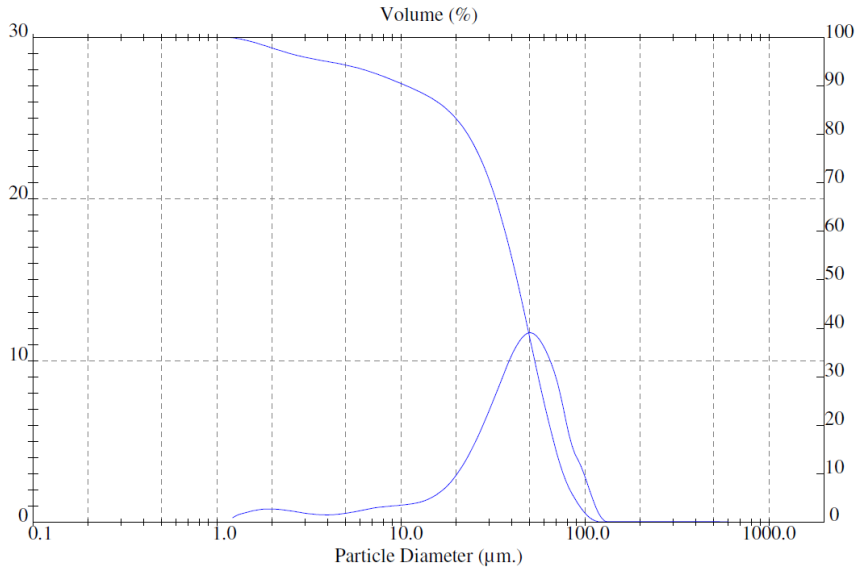

Figure 4.2: Particle size distribution of YSZ powder

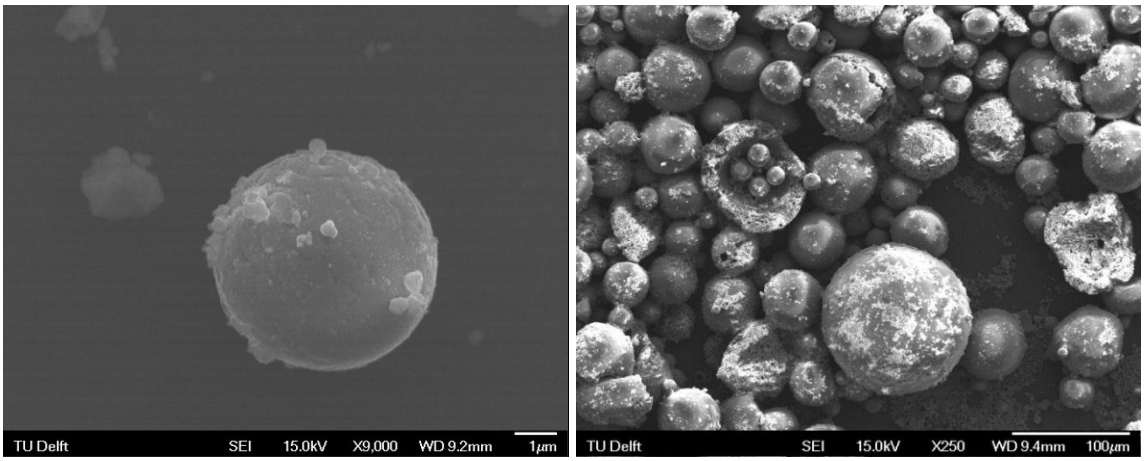

Figure 4.3: SEM images of YSZ particles

Both two types of SiO_2 powder, namely crystalline and amorphous SiO_2, were analysed by XRD to be sure of their crystallinity; see Figure 4.4. The pattern of the amorphous SiO_2 powder reveals only a broad peak at 21 degrees 2θ. The pattern of crystalline SiO_2 shows a series of distinct peaks corresponding with pure quartz.

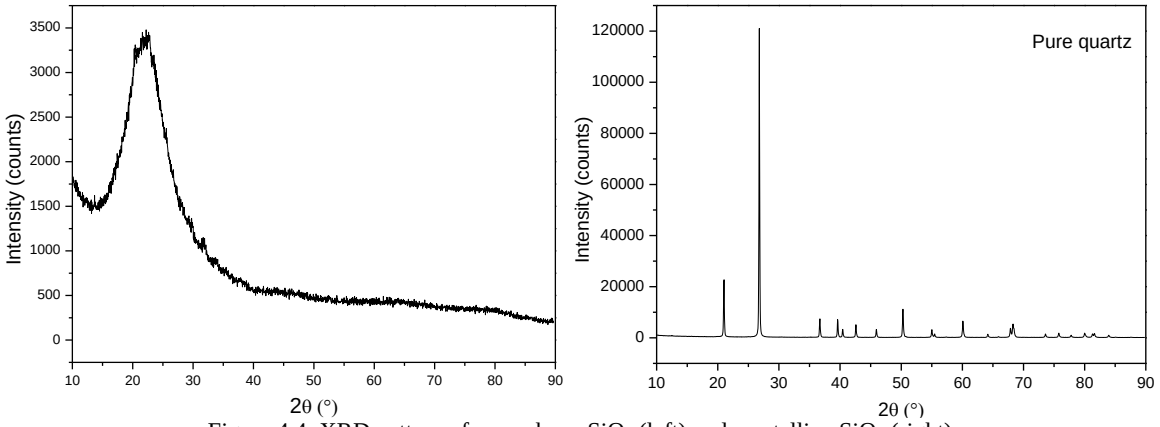

Figure 4.4: XRD pattern of amorphous SiO_2 (left) and crystalline SiO_2 (right)

The two types of $MoSi_2$ powder (cf. Section 3.1) have different particle size. The particle size of the $MoSi_2B$ powder is larger than the particle size of the $MoSi_2$ powder, with an average diameter of 18 and 5 μm, respectively; as shown in Figure 4.5 andFigure 4.6. The shape of both two $MoSi_2$ powder is irregular. Since the particle size of both two $MoSi_2$ powders is smaller than that of the YSZ powder, the $MoSi_2$ particles will fill the gap between the YSZ particles when a mixture of those particles are pressed into a tablet.

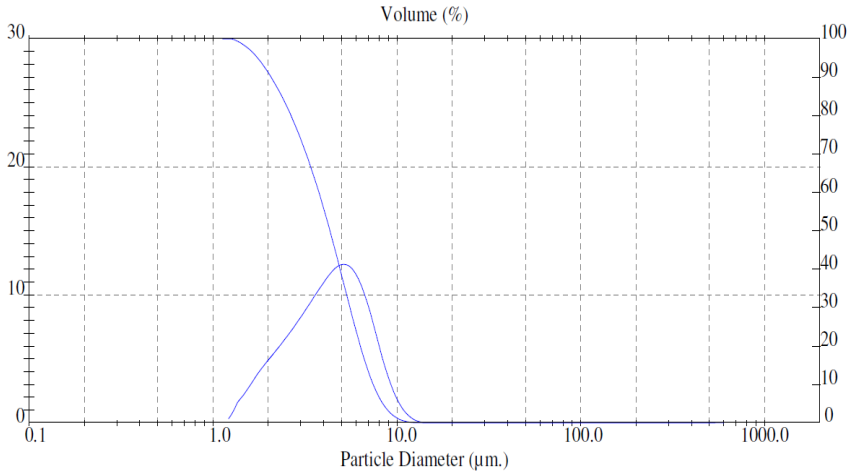

Figure 4.5: Particle size distribution of $MoSi_2$ powder

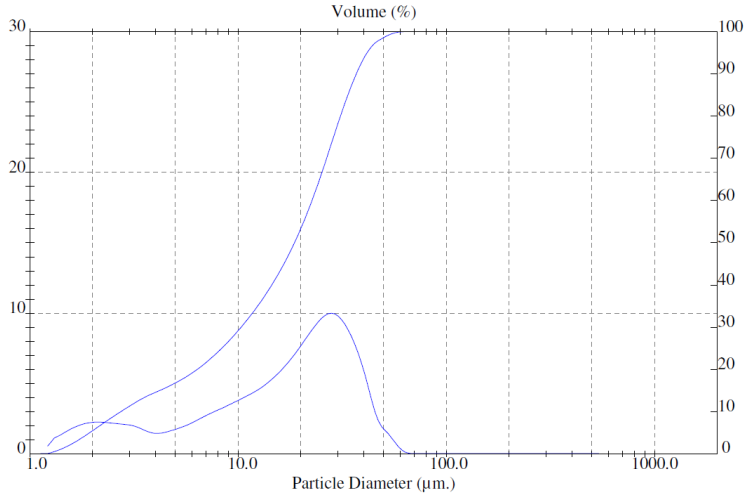

Figure 4.6: Particle size distribution of $MoSi_2B$ powder

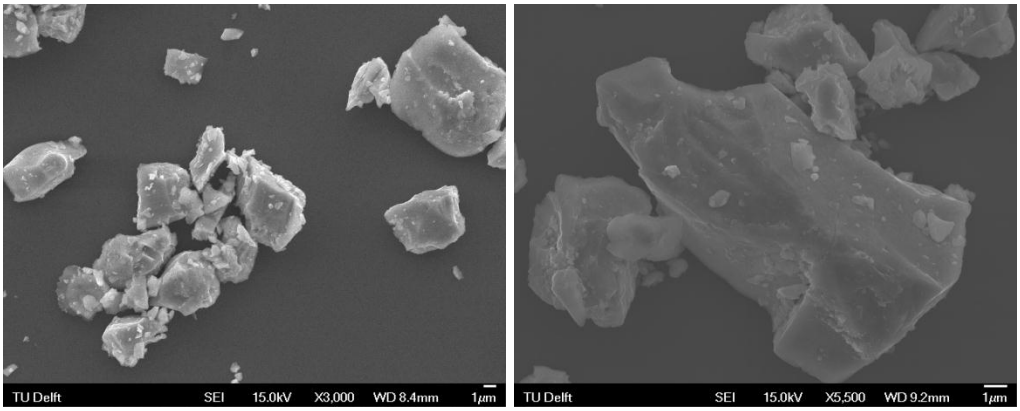

Figure 4.7: SEM image of $MoSi_2$ (left) and $MoSi_2B$ (right) particles

4.2 $ZrSiO_4$ formation from YSZ-SiO_2 mixture

Since $ZrSiO_4$ is exclusively formed from the reaction between SiO_2 and ZrO_2, the kinetics of $ZrSiO_4$ formation from a mixture of YSZ and the two types of SiO_2 powder was studied first. Tablets made from YSZ-quartz and YSZ-amorphous SiO_2 mixtures were annealed in air at 1200 °C for 15 hours. The XRD pattern of the YSZ-quartz tablet after annealing did not show any diffraction line of $ZrSiO_4$; see Figure 4.8. This result confirms the findings of Ramani [18], namely: ZrO_2 does not react with quartz. No difference in the XRD pattern of YSZ before and after annealing was observed, which means that the YSZ powder is stable and no phase transformation happens after 15 hours annealing at 1200 °C. Since a small peak corresponding with cristobalite was identified (see Figure 4.8), some of the quartz may have transformed into cristobalite after annealing.

Also no $ZrSiO_4$ was formed in YSZ-amorphous SiO_2 tablet after annealing for 15 hours in air at 1200 °C; see Figure 4.9. XRD analysis shows the amorphous SiO_2 transforms into cristobalite instead of reacting with YSZ during annealing. As already have been observed (see above) cristobalite does not react with ZrO_2 below 1300 °C [18]. The SEM image of the cross-section of the annealed tablets confirms that no reaction occurred between YSZ and cristabalite, since the integrity of the spherical YSZ powder is preserved after annealing.

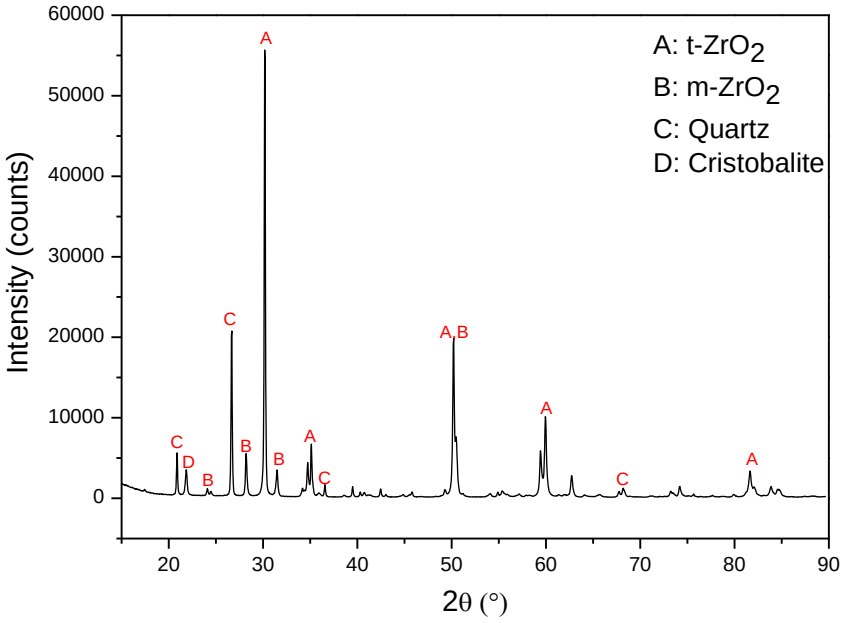

Figure 4.8: XRD pattern of YSZ-quartz tablet, annealed at 1200 °C for 15h

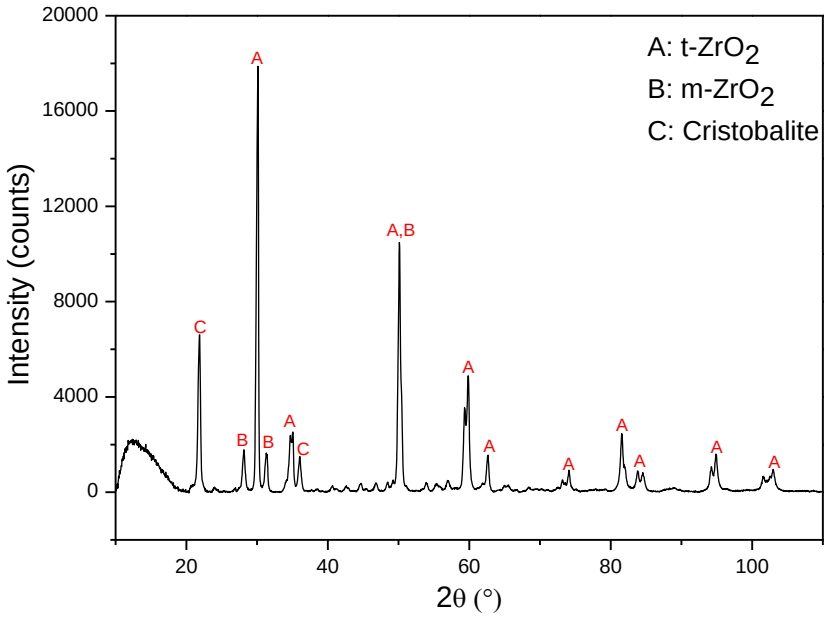

Figure 4.9: XRD pattern of YSZ-amorphous SiO_2 tablet, annealed at 1200 °C for 15h

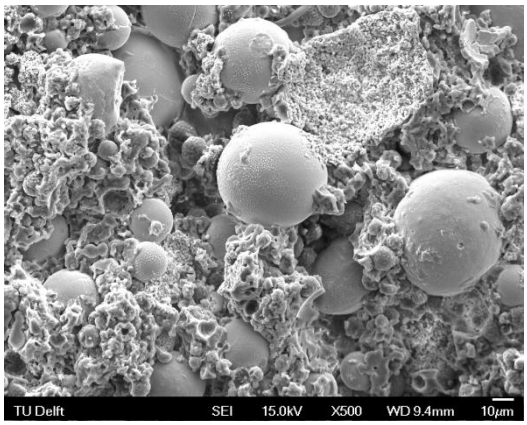

Figure 4.10: SEM image of YSZ-amorphous SiO_2 tablet, annealed at 1200 °C for 15h

Results of the previous annealing experiments clearly show that study on the kinetics of zircon formation cannot be accomplished directly using the mixtures of YSZ and SiO_2 powders. However, in a self-healing TBC based on $MoSi_2$ sacrificial particles [1] the formation of zircon has been observed [2]. Therefore, the kinetics of zircon formation is studied using YSZ-$MoSi_2$ mixtures, which will be discussed in detail in the next session.

4.3 $ZrSiO_4$ formation from YSZ-$MoSi_2$ mixtures

4.3.1 Isothermal kinetics of $ZrSiO_4$ formation at 1200 °C

The YSZ-$MoSi_2$ and YSZ-$MoSi_2$B tablets were first annealed for 15 hours in air at 1200 °C to observe any zircon formation. An evident difference between the XRD pattern of green body and annealed tablets can be seen; see Figure 4.11, 4.12 and 4.13. For both two types of tablets, the peak intensity of the zircon phase is much higher than the other phases, which indicates that zircon is formed and becomes the main phase in the sample after annealing. Other phases such as ZrO_2, $MoSi_2$ and Mo_5Si_3 exist which means that the reactants were not fully consumed. The MoO_3 formed after oxidation of $MoSi_2$ is volatile and escapes from the system during the annealing process, consequently no peaks of MoO_3 were observed in the XRD pattern. The XRD results also indicate that $MoSi_2$ as a healing agent is capable of healing cracks in YSZ through formation of $ZrSiO_4$.

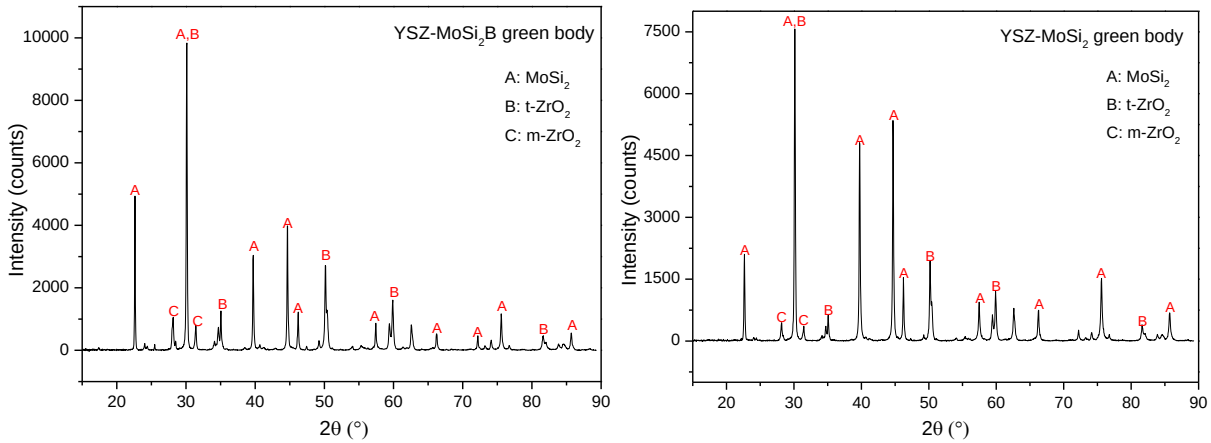

Figure 4.11: XRD pattern of YSZ-$MoSi_2$B and YSZ-$MoSi_2$ green body

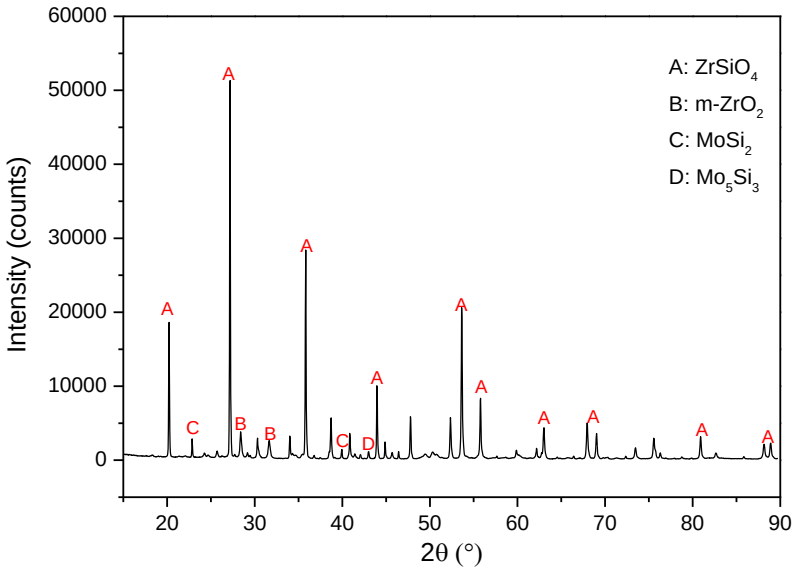

Figure 4.12: XRD pattern of YSZ-$MoSi_2$B tablets annealed at 1200 °C for 15h

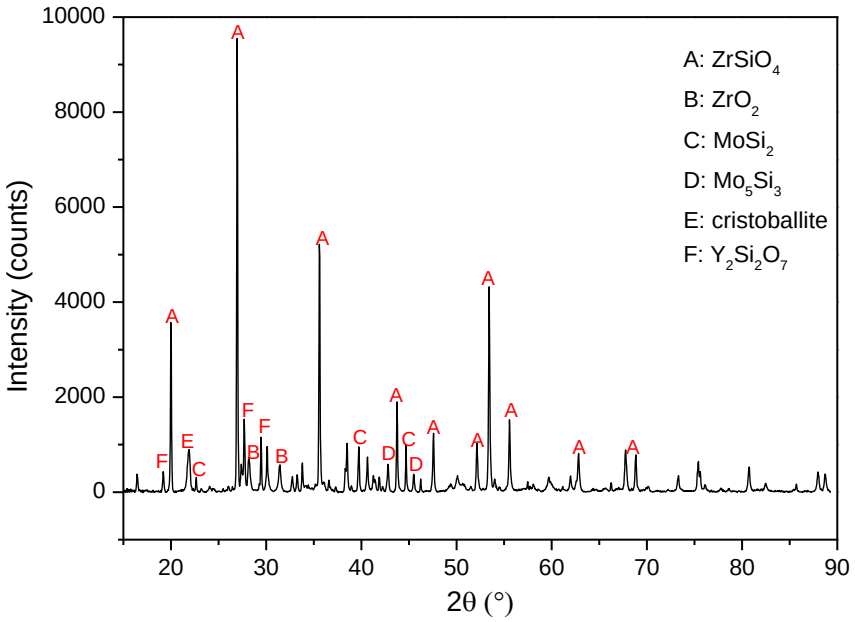

Figure 4.13: XRD pattern of YSZ-$MoSi_2$ tablet annealed at 1200 °C for 15h

The isothermal transformation of ZrO_2 into $ZrSiO_4$ for both two types of samples (with and without Boron) is shown in Figure 4.14 andFigure 4.15. Here the fraction of un-reacted ZrO_2 is plotted versus annealing time. The amount of ZrO_2 that remains in the sample is quantified using the method illustrated in Section 3.3.2. The net integrated area of $ZrSiO_4$ (200) peak is also recorded as a measure for the amount of $ZrSiO_4$ formed with annealing time. In the YSZ-$MoSi_2$B sample, ZrO_2 is consumed rapidly from the start of annealing process. The curve is steep in the early stage and flattens after about 4 hours of annealing. Therefore, it can be concluded that the reaction between ZrO_2 and the SiO_2 formed from oxidation of $MoSi_2$ is almost accomplished during the first 4 hours. The newly formed zircon does not decompose again during annealing because the dissociation reaction of zircon only occur at above 1450 °C [12]. A similar kinetic curve is also determined for the sample without Boron. The reaction rate becomes almost zero after annealing for 4 hours. However, there is an incubation time of about 0.5 hour before the rapid consumption of ZrO_2. No zircon peak is identified at 0.5 hour of annealing and the amount of ZrO_2 is practically unchanged. It is worth noting that the solid line for ZrO_2 consumption in all the figures is only to guide the eye.

The error bar due to the counting statistics of the X-ray pulse (the 2σ of total counts N equals to $2\sqrt{N}$) is also plotted in Figures 4.14 and 4.15. The size of the error bar is smaller than the symbol of each data point and thus can be neglected. The actual error is larger than the counting error of X-ray intensity.

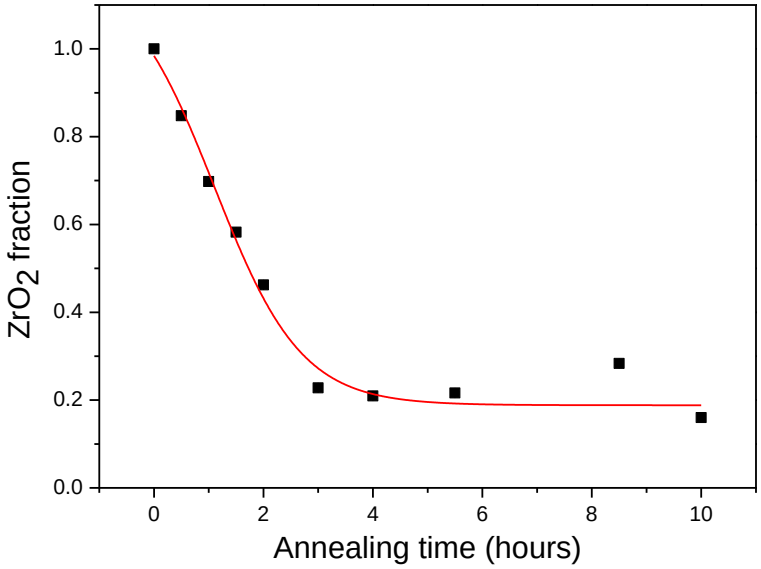

Figure 4.14: Consumption rate of ZrO_2, $MoSi_2B$ + YSZ mixture, annealed at 1200 °C

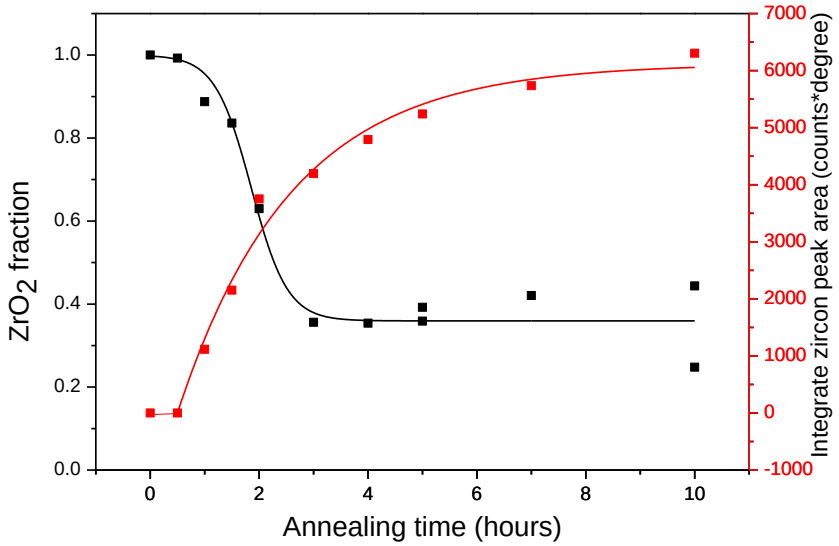

Figure 4.15: Kinetic curve of zircon formation from $MoSi_2$ + YSZ mixture, annealed at 1200 °C (red curve: zircon formation; black curve: ZrO_2 consumption)

The microstructure of the annealed tablets was analysed with SEM using cross-section of the tablets (cf. Section 3.3.3). The BSE images as shown in Figure 4.16 and Figure 4.17 provide a view on the typical microstructure of YSZ-$MoSi_2$ tablet annealed at 1200 °C in air for 15 hours. Four main phases with different element composition can be distinguished in the cross-section. Combined with X-ray microanalysis (cf. Section 3.3.3), all the phases were identified. As Si and O are the lightest element in the system, the darkest region in images is SiO_2. Since SiO_2 is exclusively formed by oxidation of $MoSi_2$, the bright "pebble-shaped" particles surrounded by SiO_2 are confirmed to be the remnant $MoSi_2$. At the edge of the $MoSi_2$ particles the Mo_5Si_3 phase is observed, which indicates that Mo_5Si_3 is formed first before further oxidation into MoO_3. The remnant ZrO_2 phase is represented by the whitish area in the BSE images. The greyish region that separates SiO_2 and ZrO_2 is the reaction product of these two reactants, namely $ZrSiO_4$.

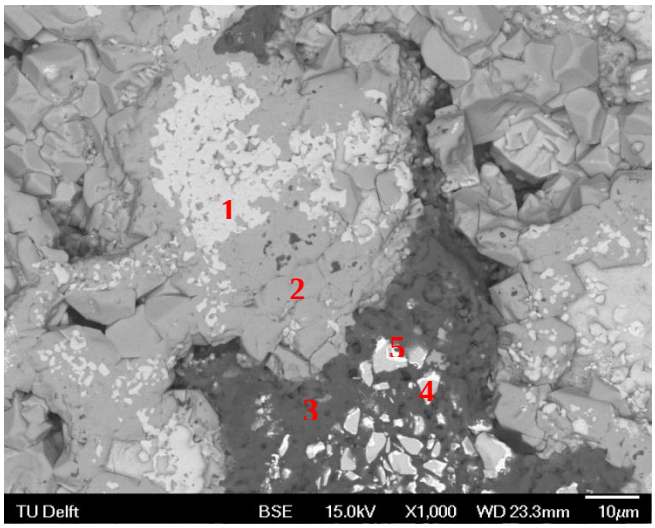

Figure 4.16: BSE image of YSZ-$MoSi_2$ tablet cross-section annealed at 1200 °C in air for 15h

Table 4.1: Results of XMA on the phases as shown in Figure 4.16

Location	Atom %			
	O	Si	Zr	Mo
1	64		36	
2	67	17	16	
3	70	30		
4		68		32
5	22	39		39

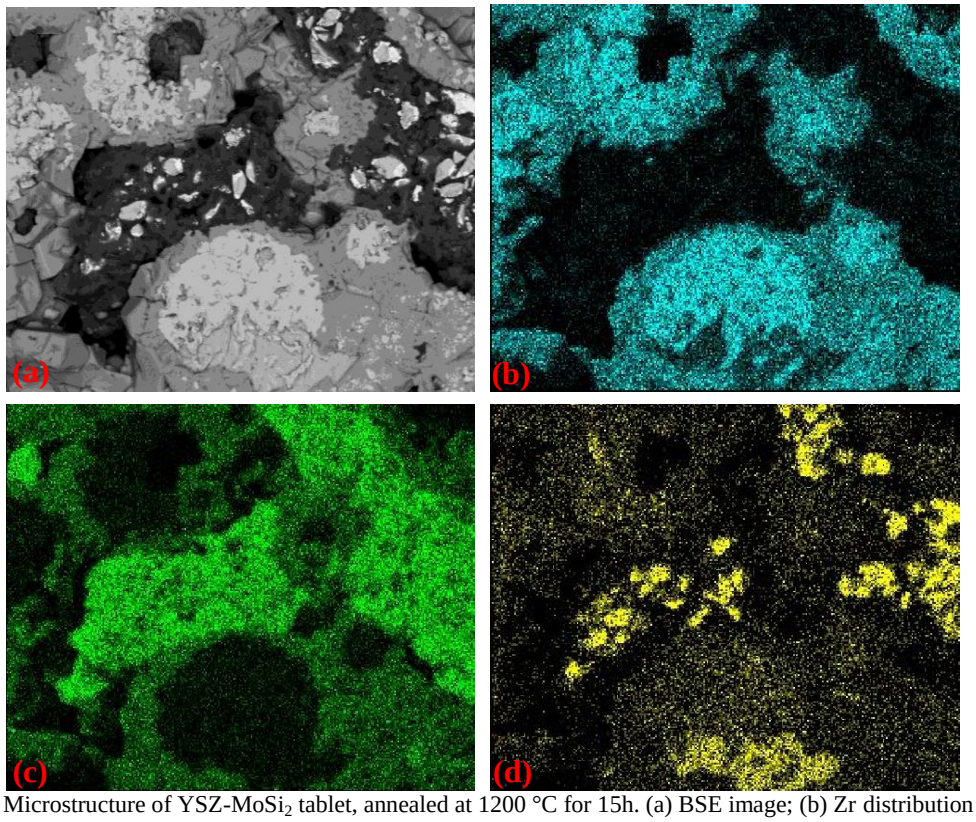

Figure 4.17: Microstructure of YSZ-$MoSi_2$ tablet, annealed at 1200 °C for 15h. (a) BSE image; (b) Zr distribution map; (c) Si distribution map; (d) Mo distribution map

The microstructure of the tablet added with Boron after annealing at 1200 °C in air is similar to the non-Boron case, as shown in Figure 4.18. The phases identified in the sample are the same as the YSZ-$MoSi_2$ sample. However, difference in the microstructure of $MoSi_2$ and SiO_2

can be clearly noticed between the two types of tablets. The size of remnant $MoSi_2$ particles in YSZ-$MoSi_2$B sample is generally larger, and the amount of SiO_2 that lies in between $ZrSiO_4$ phase and $MoSi_2$ particles is much smaller.

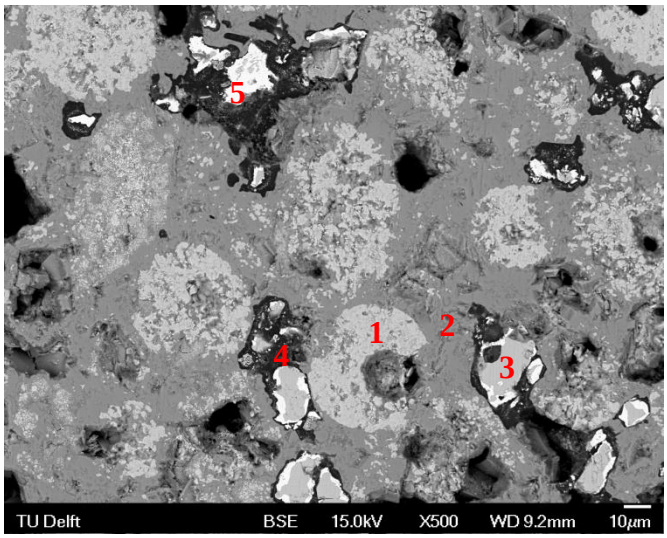

Figure 4.18: Microstructure of YSZ-$MoSi_2$(B) tablet, annealed at 1200 °C in air for 8h. (1) ZrO_2; (2) $ZrSiO_4$; (3) $MoSi_2$; (4) SiO_2; (5) Mo_5Si_3

After identifying all the phases in the SEM images, change in the microstructure and the amount of zircon formed with annealing time can then be studied. Figure 4.19 gives a qualitative comparison of the microstructure between the samples after 8 and 15 hours annealing. No significant change in the microstructure can be seen, suggesting that no further reaction between ZrO_2 and SiO_2 occurs between 8 to 15 hours. To confirm this observation, the amount of zircon needs to be determined quantitatively with the help of image analysis using the software "Image J". The volume ratio of $ZrSiO_4$ with respect to ZrO_2 in the bulk sample is the same as the ratio between the area of $ZrSiO_4$ phase and ZrO_2 phase in the SEM image. By counting the number of pixels corresponding to each phase, the amount of ZrO_2 reacted is known.

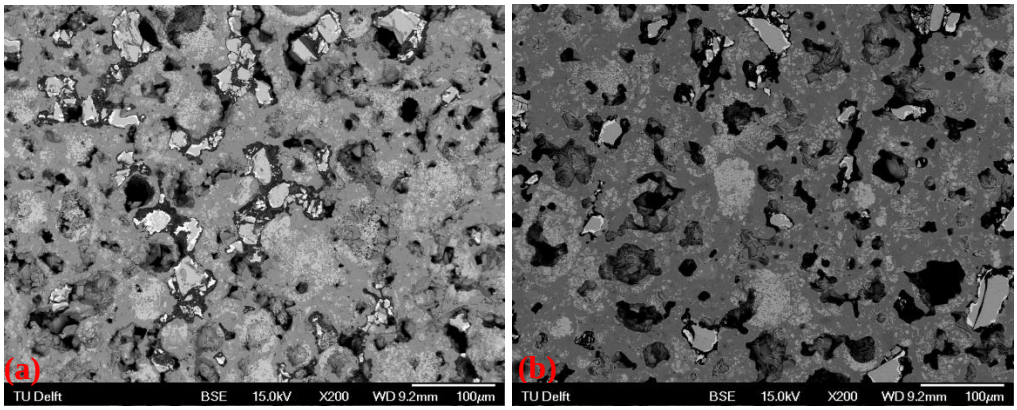

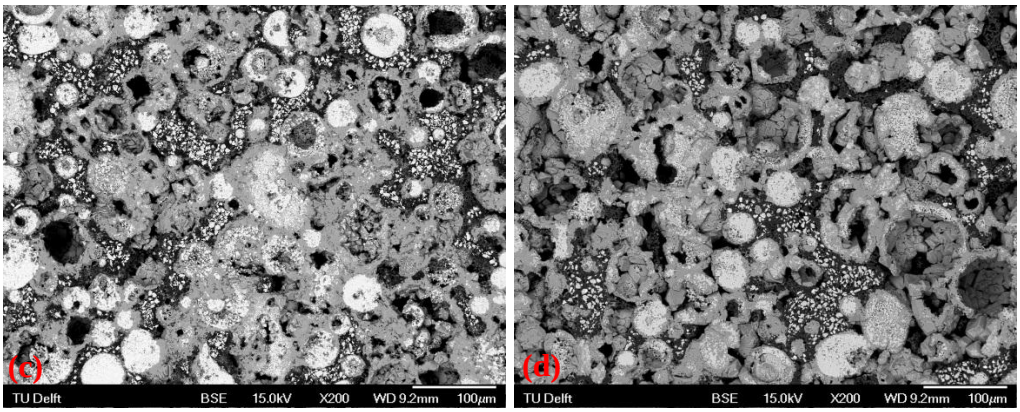

Figure 4.19: Comparison of microstructure after different annealing time. (a) YSZ-$MoSi_2B$, 8h; (b) YSZ-$MoSi_2B$, 15h; (c) YSZ-$MoSi_2$, 8h; (d) YSZ-$MoSi_2$, 15h

It is easy to distinguish ZrO_2 and $ZrSiO_4$ from the BSE images because the contrast in the grey factor between the two phases is relatively large. However, the difference of grey factor between ZrO_2 and $MoSi_2$ is small because of the similar average molecular weight of these two phases. Thus, to avoid including $MoSi_2$ phase when counting the pixels of ZrO_2, all the regions of $MoSi_2$ particles in the image were cut off and turned into black. Figure 4.20a shows an example of a BSE image modified in such way. Then the distribution of the number of pixels over the grey value in the modified image is given represented; see Figure 4.21.

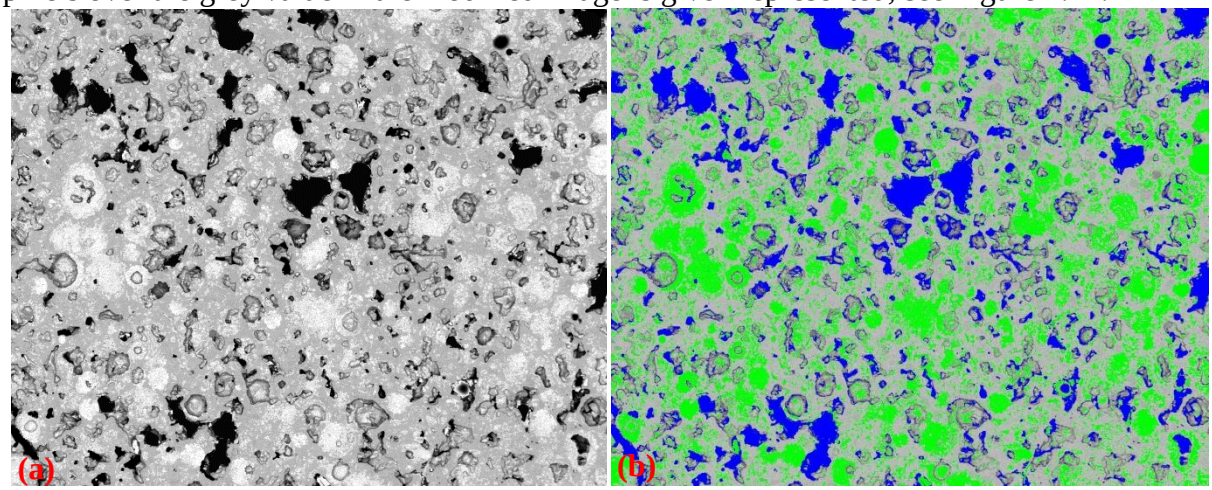

Figure 4.20: Example of image analysis on YSZ-$MoSi_2B$ sample annealed at 1200 °C for 15h: (a) modified BSE image; (b) determination of grey factor threshold of $ZrSiO_4$ phase

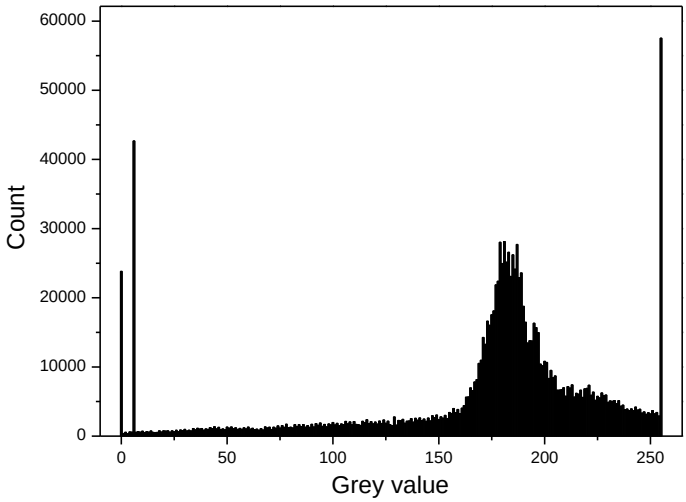

Figure 4.21: Grey value histogram of the modified BSE image (0=pure black, 255=pure white)

The image in Figure 4.20a can be further modified in a way that the pixels with grey level above a certain value are all turned into green colour while those below a certain value are changed into blue, as shown in Figure 4.20b. With this method the upper and lower grey value threshold for $ZrSiO_4$ phase in the modified BSE image can be determined manually. In this case, the grey value of zircon phase ranges roughly from 86 till 206, and the grey value for remnant ZrO_2 can be determined in the same way and ranges from 234 to 255. Then, from the histogram shown in Figure 4.21, the total number of pixels that represents $ZrSiO_4$ and ZrO_2 are calculated, and are 859257 and 136952, respectively. Hence, the ratio of the number of pixels of ZrO_2 over $ZrSiO_4$ equals 0.16, which is regarded as the same value of the volume ratio between the two phases. The volume ratio can be transformed into molar ratio by the formula:

$$\frac{m_{ZrO_2}}{m_{ZrSiO_4}} = \frac{V_{ZrO_2}}{V_{ZrSiO_4}} \times \frac{V_{m(ZrSiO_4)}}{V_{m(ZrO_2)}}$$

, where m is the number of moles, V is the real volume and V_m is the molar volume. Thus, the fraction of the ZrO_2 that is not transformed to $ZrSiO_4$ can be calculated as 23%. It is worth noting that the error in the determination of unreacted ZrO_2 fraction through "Image J" analysis comes from the selection of the boundary threshold of the grey level of each phase. Besides, the magnification of the SEM images and location in the sample where the image is taken may also result in certain error. Thus, by tuning the threshold grey level of ZrO_2 and $ZrSiO_4$ phases and analysing more than 1 image, the error of the unreacted ZrO_2 fraction is estimated to be +3% and -4%. Same method of analysis through "Image J" software is applied on the other 3 samples, with the results listed in Table 4.2.

Table 4.2: Fraction of unreacted ZrO_2 determined by "Image J" software

Sample	Fraction of unreacted ZrO_2	Range of error
YSZ+$MoSi_2B$, 1200 °C, 8h	24%	± 4%
YSZ+$MoSi_2$, 1200 °C, 8h	30%	± 2%
YSZ+$MoSi_2$, 1200 °C, 15h	27%	± 3%

The similar value for the fraction of remnant ZrO_2 determined by "Image J" analysis between 8 and 15 hours of annealing indicates that for both two samples the reaction between ZrO_2 and SiO_2 has been completed before 8 hours.

The microstructure evolution of the YSZ-$MoSi_2B$ and YSZ-$MoSi_2$ tablets during the early phase of annealing at 1200 °C in air for less than 2 hours was studied with SEM. Comparing Figure 4.22 and Figure 4.23, a significant change in microstructure can be witnessed in the YSZ-$MoSi_2B$ samples. Most of the ZrO_2 particles are intact and remains their spherical shape after 0.5 hours of annealing. The $ZrSiO_4$ phase is observed only at very few ZrO_2 particles near the surface of the tablet. While after annealing for 2 hours, the zircon phase can be detected throughout the whole sample and no unreacted ZrO_2 particles were observed. This is consistent with the rapid consumption of ZrO_2 as follows from the kinetic curve determined by XRD during the first 2 hours of annealing; see Figure 4.14. SiO_2 is formed due to the oxidation of $MoSi_2$ and can fully wet the surface of ZrO_2 particles after 0.5 hours of annealing. Thus, ZrO_2 is in good contact with SiO_2 from the beginning of annealing process. This indicates that rate of zircon formation only depends on the rate of reaction between ZrO_2 and SiO_2 instead of $MoSi_2B$ oxidation.

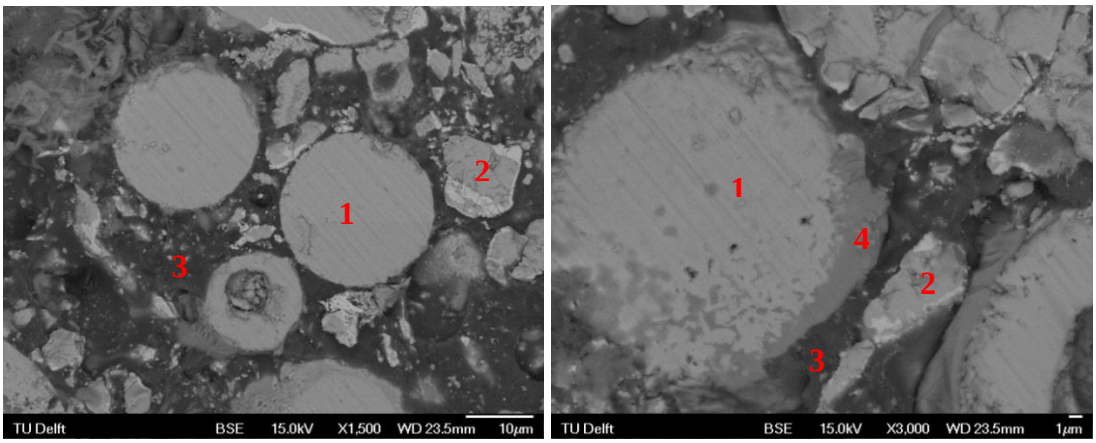

Figure 4.22: BSE images of YSZ- $MoSi_2B$ tablet annealed at 1200 °C for 0.5 hour, (1) ZrO_2; (2) $MoSi_2$; (3) SiO_2; (4) $ZrSiO_4$

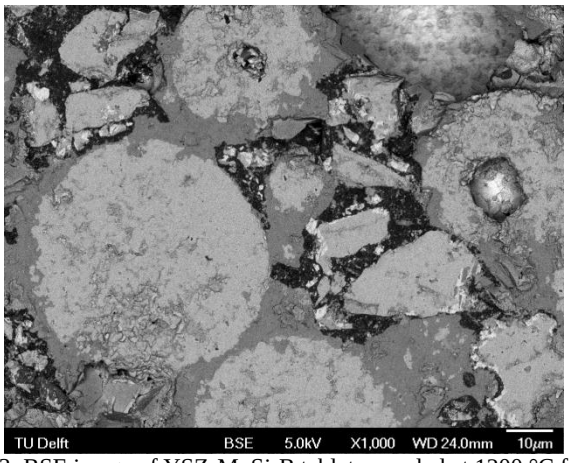

Figure 4.23: BSE image of YSZ-$MoSi_2B$ tablet annealed at 1200 °C for 2 hours

A significant change of the microstructure of YSZ-$MoSi_2$ tablet between 1 and 2 hours of annealing is observed in the SEM images; see Figures 4.24 and 4.25. The shape of the ZrO_2 particles in the sample remains intact after annealing for 1 hour. No evident oxidation of $MoSi_2$ occurs yet since the original morphology of the $MoSi_2$ particles can still be recognized and little amount of SiO_2 can be observed. The difference in the grey level in the BSE image between the interior and the surface of ZrO_2 particles indicates that Si atoms have already diffused into ZrO_2. The $ZrSiO_4$ phase can hardly be identified except at the surface of some certain ZrO_2 particles; see Figure 4.24. However, after two hours of annealing, large amount of SiO_2 is formed and fill the space between particles. $ZrSiO_4$ is identified clearly at the interface between SiO_2 and ZrO_2; see Figure 4.25. The rapid loss of ZrO_2 during the annealing from 1 to 2 hours determined by XRD is substantiated by the SEM analysis.

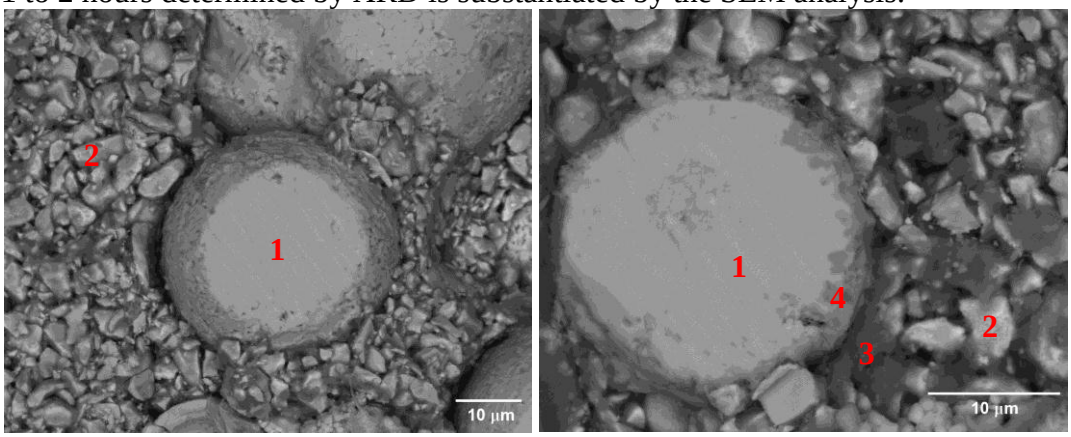

Figure 4.24: BSE images of YSZ- $MoSi_2$ tablet annealed at 1200 °C for 1 hour, (1) ZrO_2; (2) $MoSi_2$; (3) SiO_2; (4) $ZrSiO_4$

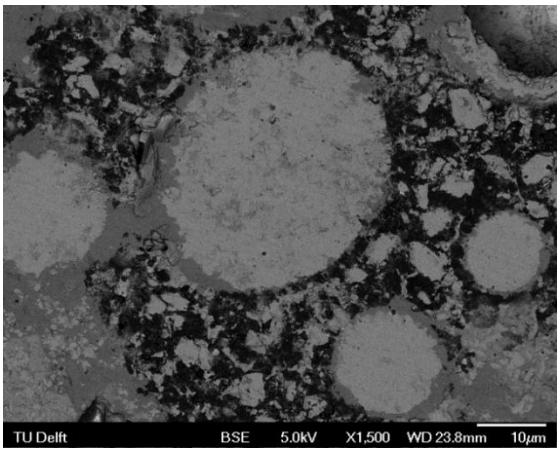

Figure 4.25: BSE image of YSZ-$MoSi_2$ tablet annealed at 1200 °C for 2 hours

4.3.2 Isothermal kinetics of $ZrSiO_4$ formation at 1100 °C

The XRD results proved that $ZrSiO_4$ can be formed by annealing of both two types of YSZ-$MoSi_2$ mixtures at 1100 °C in air; see Figure 4.26 and 4.27. The kinetics of the $ZrSiO_4$ formation at 1100 °C in air is determined; see Figures 4.28 and 4.29. For both two types of YSZ-$MoSi_2$ mixtures, the reaction between YSZ and SiO_2 stops before 15 hours. The amount of remnant ZrO_2 in the system is much higher than that when annealing at 1200 °C, as can be seen also from the relative peak intensity between $ZrSiO_4$ phase and ZrO_2 phase in the XRD patterns; see Figures 4.26, 4.27,Figure 4.12 andFigure 4.13. When Boron is added, ZrO_2 reacts with SiO_2 rapidly from the start of annealing, as proved by the significant loss in ZrO_2 after annealing for 1 hour. The reaction rate slows down after 1 hour and becomes almost zero after 8 hours. For the mixture without Boron, no rapid consumption of ZrO_2 is observed during the early stages of annealing. The reaction proceeds slowly and almost finishes after 10 hours. Judged from the initial kinetic behaviour of the YSZ-$MoSi_2$ mixture annealed at 1200 °C, an incubation period for the ZrO_2-SiO_2 reaction is also expected at 1100 °C when Boron is absent. At the lower temperature, it is reasonable to assume that the incubation time is longer.

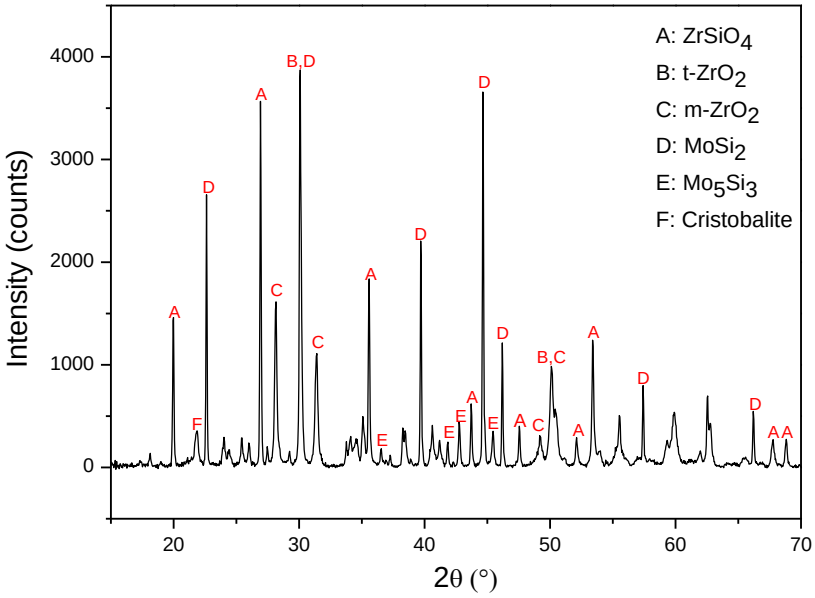

Figure 4.26: XRD pattern of YSZ-$MoSi_2$B tablets annealed at 1100 °C for 15h

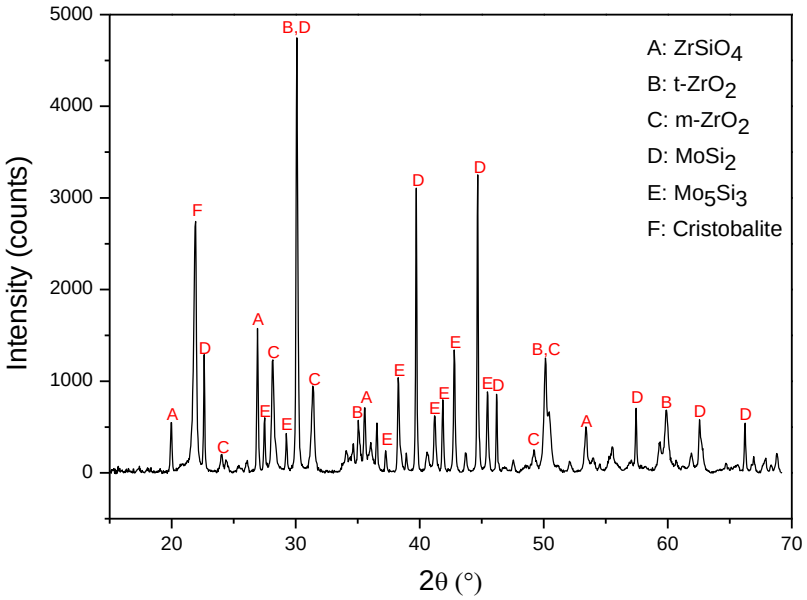

Figure 4.27: XRD pattern of YSZ-$MoSi_2$ tablets annealed at 1100 °C for 15h

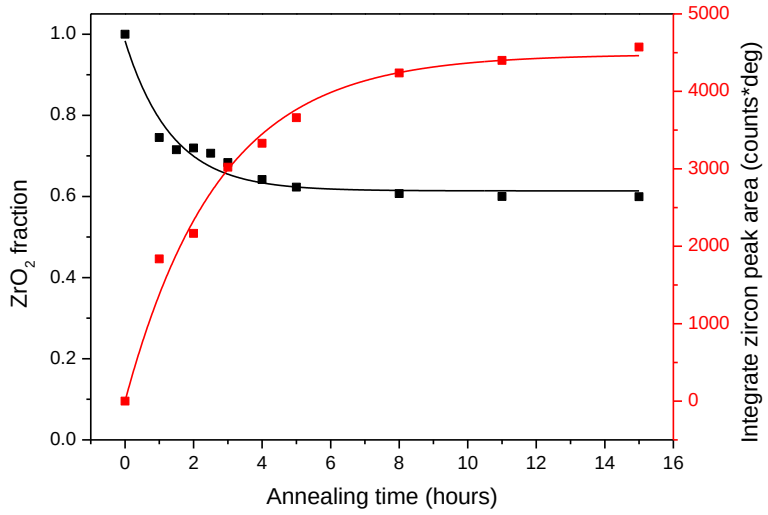

Figure 4.28: Kinetic curve of zircon formation from YSZ + $MoSi_2$B mixture, annealed at 1100 °C (red curve: zircon formation; black curve: ZrO_2 consumption)

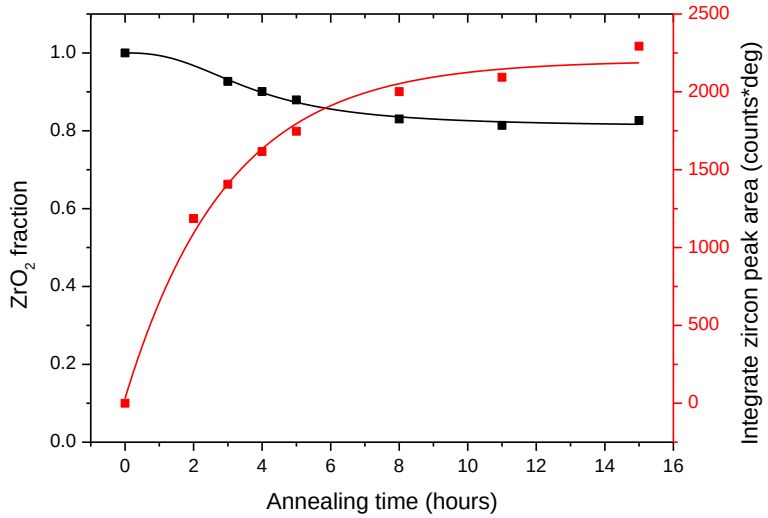

Figure 4.29: Kinetic curve of zircon formation from YSZ + $MoSi_2$ mixture, annealed at 1100 °C (red curve: zircon formation; black curve: ZrO_2 consumption)

The microstructure of the YSZ-$MoSi_2B$ tablet after annealing at 1100 °C for 15 hours is similar to the one annealed at 1200 °C for 2 hours; see Figure 4.23 and 4.30. The SiO_2 formed from the oxidation of $MoSi_2$ can fill the space between particles and wet the surface of ZrO_2 particles very well. $ZrSiO_4$ is formed at the peripheral of ZrO_2 particles and can be identified clearly in the BSE images. Other phases, such as Mo_5Si_3 and remnant $MoSi_2$, are also detected, which confirms the XRD results.

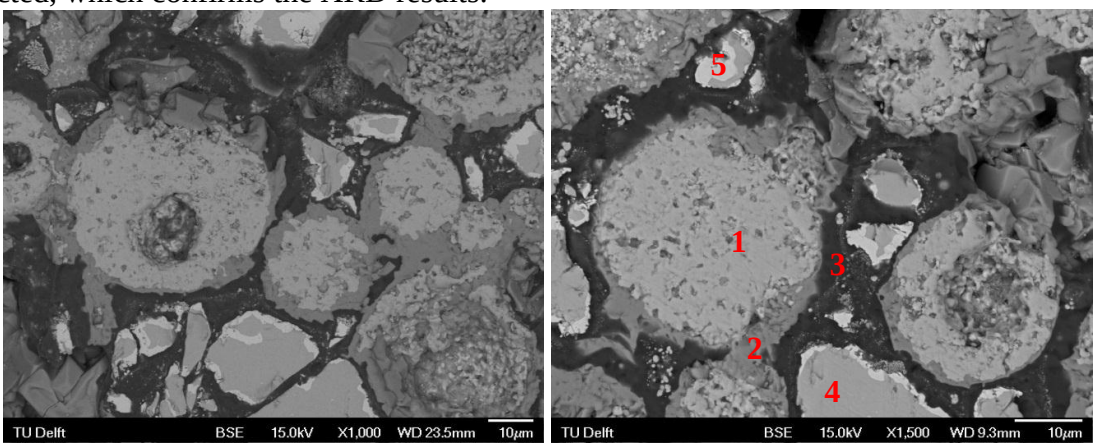

Figure 4.30: BSE images of YSZ-$MoSi_2B$ tablet annealed at 1100 °C for 15 hours. (1) ZrO_2; (2) $ZrSiO_4$; (3) SiO_2; (4) $MoSi_2$; (5) Mo_5Si_3

4.3.3 Estimation of the rate of zircon formation

The rate of $ZrSiO_4$ formation at the start of ZrO_2-SiO_2 reaction is quantified. As shown in Figure 4.15, Figure 4.28 andFigure 4.29 (red curve), the kinetics of zircon formation can be represented by the formula [25]:

$$y = a[1-\exp(-kt)] \qquad (4.1)$$

, where k is the reaction constant, and a is the maximum vertical value of the fitted curve (in this case a represents the integrated zircon peak area). The value of k and a can be directly obtained from the software "Origin" by fitting Equation (4.1) to the experimental data. The reaction rate decreases with annealing time. By differentiating equation (4.1), the initial reaction rate can be expressed as:

$$\left.\frac{dy}{dt}\right|_{t=0} = ak \qquad (4.2)$$

From the data in Table 4.2, the amount of $ZrSiO_4$ in the sample (i.e. YSZ+$MoSi_2$ tablet annealed at 1200 °C) can be related to the integrate area of $ZrSiO_2$ peak in XRD pattern (i.e. the value of a). Thus, the reaction rate can be expressed in the unit of mol/hour per tablet. Since the parameters of all the XRD measurement are the same, and by assuming that all the samples have the same density with $ZrSiO_4$ phase homogeneously distributed, the value of the initial reaction rate of the samples annealed at 1100 °C can also be estimated and compared. The results are listed in Table 4.3.

The data that corresponds with $ZrSiO_4$ formation for the YSZ-$MoSi_2B$ sample annealed at 1200 °C is not considered due to an instrumental defect. As a result, the rate of $ZrSiO_4$ formation of this sample is determined from the consumption rate of ZrO_2. The rate constant k_G in this case represents the rate of the shrinkage of the YSZ particle diameter (cf. Section 2.7), and its value can be acquired from the slope of the line that fit the conversion function of volume contraction model to the experimental data; cf. Figure 4.45 and Section 4.5. The total surface area of all the YSZ particles is needed to determine the initial rate of zircon formation.

It is assumed that all the YSZ particles in the sample have the same average diameter of 50 μm.

Table 4.3: Comparison of the initial reaction rate in different samples

Samples	Annealing temperature (°C)	*a* (degree×counts)	k (h^{-1})	k_G (μm/h) [2]	Reaction rate (mol/h)
YSZ+$MoSi_2B$	1200	-	-	2.75	0.0014
	1100	4479	0.37	-	0.00081
YSZ+$MoSi_2$	1200	6121	0.47	-	0.0015
	1100	2197	0.34	-	0.00037

4.3.4 Discussion on the kinetics of self-healing reaction of $MoSi_2$ and $MoSi_2B$ healing particles

The experimental results given in Session 4.3 has proven that the envisioned principle of the self-healing process in thermal barrier coatings can be accomplished by using $MoSi_2$ and $MoSi_2B$ as sacrificial healing particles; cf. Chapter 1. In view of this application, the isothermal kinetics of $ZrSiO_4$ formation from the YSZ-$MoSi_2$ and YSZ-$MoSi_2B$ mixtures annealed at 1200 and 1100 °C in air will be discussed.

Difference in the kinetic behaviour of YSZ-$MoSi_2$ system between 1200 and 1100 °C is first compared. At both temperatures an incubation time exists because of the relatively low oxidation rate of $MoSi_2$ during the initial period. The amount of SiO_2 formed is too low to make full contact or react with ZrO_2 at early stage, as indicated from the SEM image in Figure 4.24. The reaction between ZrO_2 and SiO_2 below 1676 °C is thermodynamically favourable, and the molar ratio between Zr and Si in the system is one. Thus it is expected that the ZrO_2 will be fully consumed after reaction. However, the amount of remnant ZrO_2 in the system after 15 hours of annealing at 1200 °C reaches about 30 %. This may be explained as follows. Firstly, the reaction product, namely zircon, which separates the ZrO_2 and SiO_2, becomes a barrier for the diffusion of reactant species (e.g. oxygen vacancies, Si ions, electrons) when its thickness is large. Secondly, the YSZ raw powder is composed by both tetragonal and monoclinic phase, and the reaction rate for tetragonal ZrO_2 is likely to be much faster than that of monoclinic ZrO_2 as indicated by the change in the ratio of peak intensity between tetragonal and monoclinic ZrO_2 in the XRD pattern before and after annealing (see Figure 4.11 and Figure 4.13). Thirdly, part of the amorphous SiO_2 transforms into cristobalite during annealing (see Figure 4.13), and crystalline SiO_2 does not react with ZrO_2. When the annealing temperature is 1100 °C, the rate of ZrO_2-SiO_2 reaction drops significantly. There is a large increase in the amount of remnant ZrO_2 when lowering the annealing temperature. This can be explained by the large transformation of amorphous SiO_2 into cristoballite, which is proved by the high peak intensity of cristoballite phase shown in Figure 4.27.

The addition of Boron in the $MoSi_2$ powder effectively influences the kinetics of zircon formation. For both annealing temperatures of 1200 and 1100 °C, no incubation time is observed in the kinetics curve in YSZ-$MoSi_2B$ system. The reaction between ZrO_2 and SiO_2 starts rapidly from the beginning of annealing. The formation of SiO_2 from the oxidation of $MoSi_2$ is faster when Boron is added, which can be clearly seen from the comparison between the SEM images of the two tablets at early phase of annealing (see Figure 4.22 and Figure

[2] Since no data are available for $ZrSiO_4$ peak intensities (see text for details), the reaction rate is estimated on the basis of the volume contraction model (see Section 2.7)

4.24). It is interesting to find that at 1100 °C the initial rate of $ZrSiO_4$ formation in YSZ-$MoSi_2B$ sample is almost twice as that in the YSZ-$MoSi_2$ sample. This indicates the better capability of $MoSi_2B$ particles in rapid healing than that of $MoSi_2$ particles at lower temperature. The effect of Boron on the crystallinity of the SiO_2 formed is proved. The addition of Boron promotes the formation of amorphous SiO_2 and postpones the transition of SiO_2 from amorphous state to cristobalite. This can be clearly determined from the peak intensity of cristabalite in the XRD patterns of YSZ-$MoSi_2$ and YSZ-$MoSi_2B$ system after 15 hours annealing at both 1100 and 1200 °C; cf. Figure 4.12, Figure 4.13, Figure 4.26 and Figure 4.27. The crystallization of SiO_2 does not occur before the completion of its reaction with ZrO_2 at 1200 °C when boron is added. This can also explain the result that the fraction of remnant ZrO_2 is lower when Boron is added, especially at 1100 °C.

The effect of Boron and annealing temperature can also be revealed considering the initial rate of the chemical reaction between YSZ and amorphous SiO_2; see Table 4.3. As expected, the reaction rate constant *k* increases with temperature. The reaction rate constant *k* in the YSZ-$MoSi_2B$ tablet is close to that of YSZ-$MoSi_2$ tablet at 1100 °C, whereas there is a large difference in the formation rate of zircon between the two samples. This suggests that the rate of chemical reaction between YSZ and amorphous SiO_2 itself is not influenced by Boron. However, the addition of Boron increases the amount of amorphous SiO_2 (cf. Section 4.3.2) so that the contact area between YSZ and amorphous SiO_2 is higher, and this leads to the higher formation rate of zircon.

The images of the microstructure of the YSZ-$MoSi_2B$ tablet annealed for 0.5 hours at 1200 °C provide qualitative information on the self-healing capability of $MoSi_2B$ healing particles. The amorphous SiO_2 formed from the oxidation of $MoSi_2B$ has good wettability. As shown in Figure 4.31a, the SiO_2 fills the crack inside one ZrO_2 particle, and zircon is formed at the interface of SiO_2 and ZrO_2. At some region all the SiO_2 that fills the crack is consumed and $ZrSiO_4$ connects the two neighbouring ZrO_2 particles. Similarly, Figure 4.31b shows another example of the connection between two ZrO_2 particles by the formation of $ZrSiO_4$. The minimum size of the gap between the two particles is estimated to be 0.8 μm from the SEM image. The interface between ZrO_2 and $ZrSiO_4$ shows good bonding between the two phases, and no sign of delamination was observed. Therefore it is anticipated that a good mechanical integrity of TBC after crack healing can be achieved.

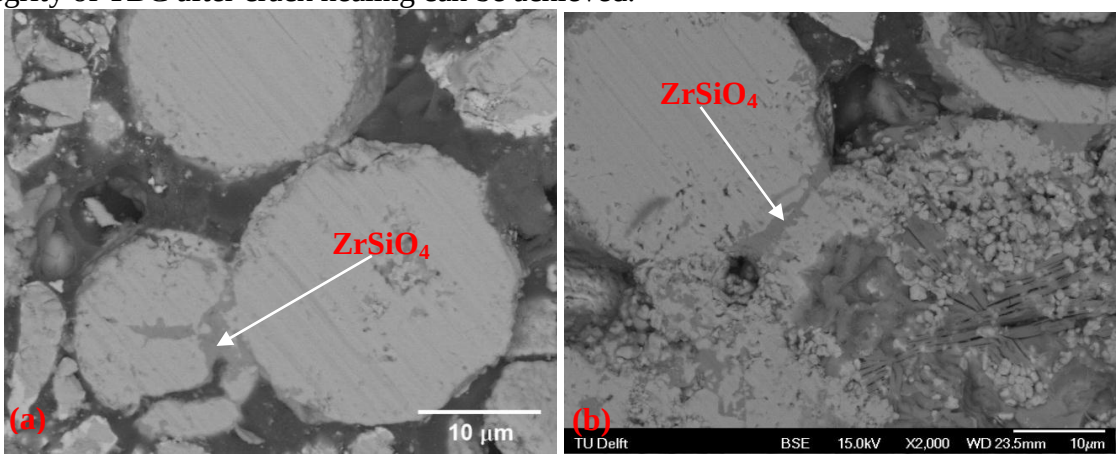

Figure 4.31: BSE images of YSZ-$MoSi_2B$ annealed for 0.5 hours at 1200 °C

Since the reactions in YSZ-$MoSi_2$ (with and without Boron) mixtures is rather complex, chemical reactions that is not self-healing related also occur during annealing process and some by-products are formed. As shown in Figure 4.32, a phase with grey level between ZrO_2 and $ZrSiO_4$ can be found near the remnant ZrO_2. This reaction by-product is identified as a Y-

Mo-O compound from the X-ray microanalysis. However, such Y-Mo-O phase cannot be seen in the XRD patterns. From the LPF database [31] of Y-Mo-O compound, it is found that diffraction peaks of $Y_2Mo_2O_7$ and $Y_{0.44}Mo_{0.56}O_{1.78}$ overlap with those of tetragonal ZrO_2, and their crystal structure and lattice parameter are similar to ZrO_2. Further, $Y_2Si_2O_7$ is found only in YSZ-$MoSi_2$ sample at 1200 °C annealing; see Figure 4.13. The amount of these by-product phases formed is relatively small, and thus they are not supposed to have a large influence on the $ZrSiO_4$ formation.

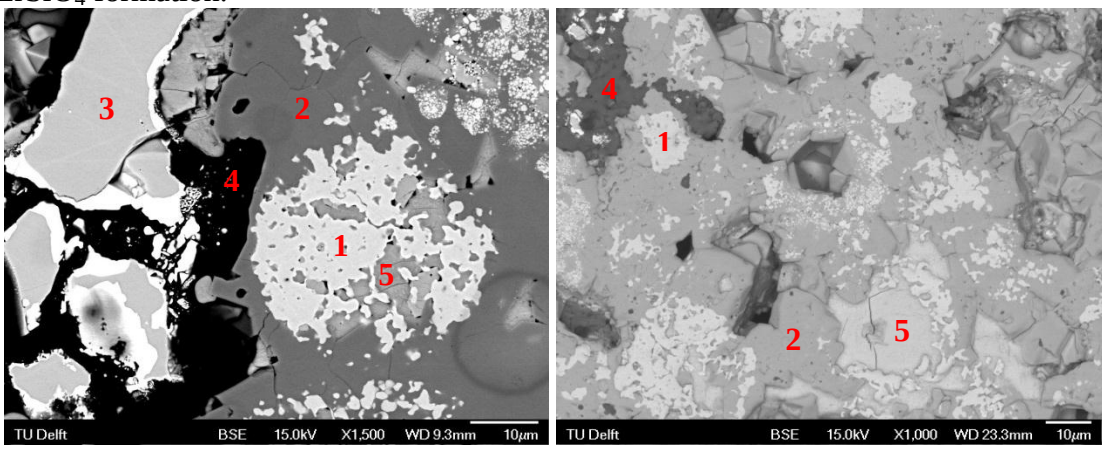

Figure 4.32: BSE image of YSZ-$MoSi_2B$ (left) and YSZ-$MoSi_2$ (right) annealed at 1200 °C for 15 hours, (1) ZrO_2; (2) $ZrSiO_4$; (3) $MoSi_2$; (4) SiO_2; (5) Y-Mo-O compound

4.4 Thermal analysis

4.4.1 Thermal behaviour of $MoSi_2$ and $MoSi_2B$ powder annealed in synthetic air

The result of thermal analysis on the $MoSi_2$ powder is shown in Figure 4.33. DTA and TG curves are plotted against sample temperature for a constant heating rate of 5 °C/min. The thermal behaviour of $MoSi_2$ oxidized in air can be interpreted as follows. Oxidation of $MoSi_2$ starts at about 400 °C and ends before 600 °C, as proved by the significant exothermic peak together with a dramatic increase in the weight of sample. At around 800 °C the mass of the sample suddenly drops. This can be explained by the evaporation of the volatile MoO_3 above 800 °C. The heat effect of such evaporation is relatively small, since only a slight peak is shown in DTA curve at 800 °C. No significant reaction or phase transformation in the sample happened at high temperature region (i.e. above 900 °C), because no evident deviation from the baseline of DTA and TG curve is observed.

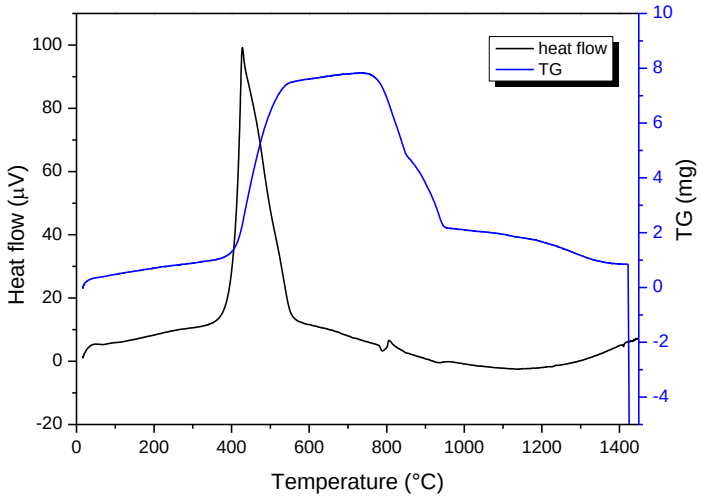

Figure 4.33: DTA and TG result on $MoSi_2$ powder, heating rate 5 °C/min

The result of XRD analysis of the $MoSi_2$ sample after DTA experiment is given in Figure 4.34. The $MoSi_2$ powder is not fully oxidized, and the major phase still is $MoSi_2$. Mo_5Si_3 is formed as one of the oxidation products. The cristobalite peak is identified, which means that some of the SiO_2 formed from $MoSi_2$ oxidation is crystalized. No MoO_3 peaks are identified, which indicates that MoO_3 totally escapes the system after evaporation.

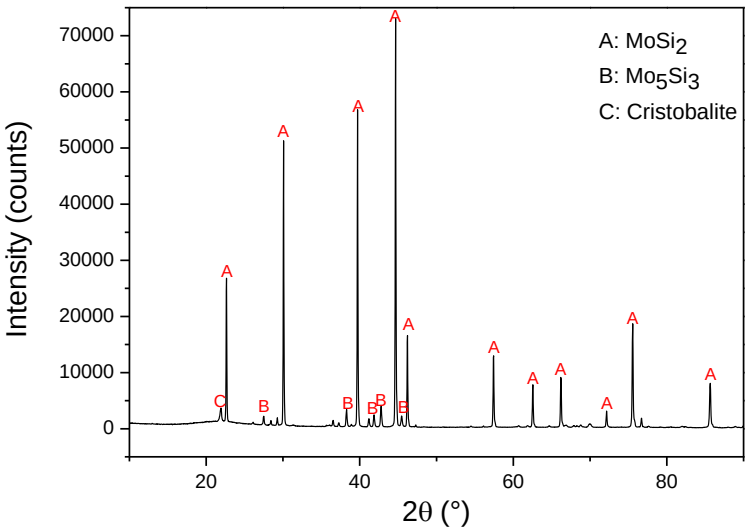

Figure 4.34: XRD pattern of $MoSi_2$ powder after DTA measurement

The DTA/TG result for the $MoSi_2B$ powder is given in Figure 4.35. The thermal behaviour of $MoSi_2B$ sample in the low temperature region is similar to that of $MoSi_2$. An exothermal peak due to $MoSi_2$ oxidation is observed between 400 to 600 °C. The mass of the sample increases continuously from 400 °C until 800 °C, followed by a sudden drop due to the evaporation of MoO_3. However, in the case of $MoSi_2B$ powder, there is a very sharp peak near 800 °C. Normally, such peaks correspond to melting in DTA curve, because it occurs over a narrow temperature interval [24]. Thus it can be falsely believed that this sharp peak at 800 °C is related to the melting and evaporation of MoO_3. The melting and evaporation is an endothermic process (i.e. peak should point to negative value in the DTA curve). Therefore, the exothermic peak at 800 °C must be the result of another thermal event in the system (e.g. oxidation and evaporation of Boron), and the nature of this thermal event is unknown yet.

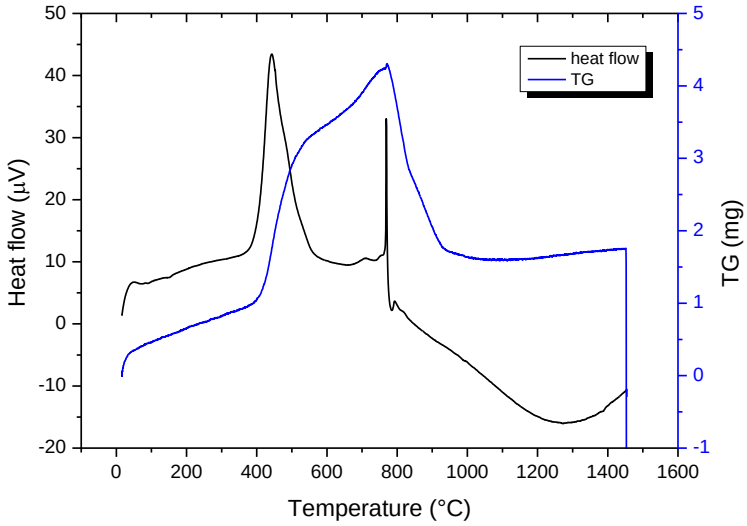

Figure 4.35: DTA and TG result on $MoSi_2B$ powder, heating rate 5 °C/min

The XRD pattern of $MoSi_2B$ powder after DTA measurement shows that the $MoSi_2$ is not fully consumed in the oxidation process; see Figure 4.36. All the MoO_3 formed during oxidation has escaped the system. The difference with the XRD pattern of $MoSi_2$ sample is that no Mo_5Si_3 peaks are identified. Thus it is believed that the oxidation rate of Mo_5Si_3 is fast. Moreover, Boron is not fully oxidized and still exists in the sample after thermal measurement. Most importantly, no cristobalite is found which indicates that the addition of Boron in the $MoSi_2$ powder promotes the amorphous state of SiO_2 effectively.

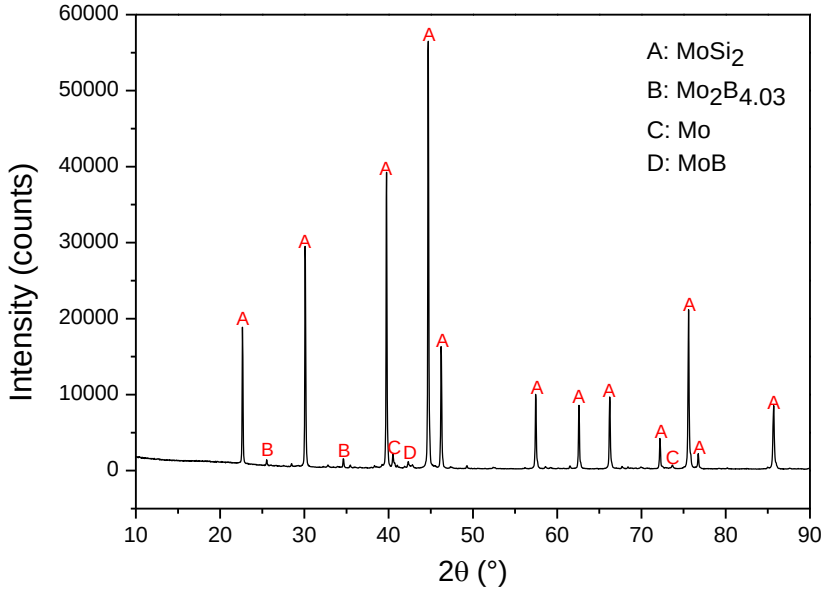

Figure 4.36: XRD pattern of $MoSi_2B$ powder after DTA measurement

4.4.2 Determination of the activation energy of $MoSi_2$ and $MoSi_2B$ oxidation

Since the peak position in DTA curve shifts to higher temperature with increasing heating rate, the activation energy of the $MoSi_2$ oxidation process can be determined by the Kissinger method as illustrated in Section 2.5. To this end, $\ln(\beta/T_p^2)$ is plotted against $1/T_p$ as shown in Figure 4.37. By linear fitting the four data points, the slope of the line is estimated to be -9061. Using Equation (1.12), the activation energy for the oxidation of $MoSi_2B$ sample is determined as 75^{+8}_{-10} kJ/mol. It is worth noting that the error in determination of T_p leads to the error bar of the data points in horizontal axis in the Kissinger plot, while the vertical error is within 0.3% (i.e. the vertical error bar is the same size as the symbol in the plot) and thus can be neglected. With the Ozawa method, the activation energy calculated is 79^{+7}_{-12} kJ/mol.

The activation energy of the oxidation process of $MoSi_2$ sample is determined in the same manner; see Figure 4.38. The activation energy determined by Kissinger and Ozawa method is 64^{+22}_{-14} and 68^{+11}_{-19} kJ/mol, respectively. Unlike the $MoSi_2B$ sample, the result of $MoSi_2$ sample shows that the deviation of two data points from the linear fitted line is larger than experimental error.

The activation energy of the oxidation of $MoSi_2B$ and $MoSi_2$ powder are close, which means that the rate of the oxidation of $MoSi_2B$ is similar to that of $MoSi_2$. However, this is not consistent with the result observed from SEM images of YSZ-$MoSi_2B$ and YSZ-$MoSi_2$ tablets during early period of annealing (see Figure 4.22 and Figure 4.24). The particle size of $MoSi_2$ powder is smaller than that of $MoSi_2B$ powder, and thus the frequency factor of the oxidation

of $MoSi_2$ powder is expected to be higher than $MoSi_2B$ powder. The experiment procedure on both two systems, namely with and without Boron, is the same in all experiments. Therefore it is speculated that the existence of ZrO_2 influence the oxidation kinetics of $MoSi_2$ and $MoSi_2B$.

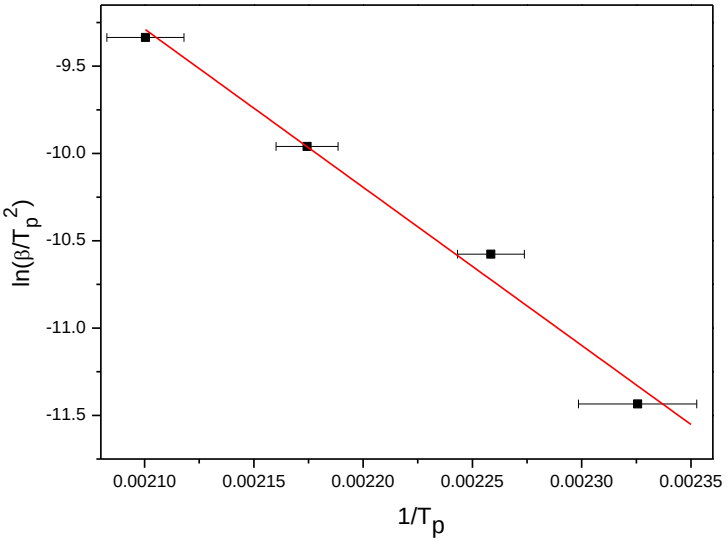

Figure 4.37: Determination of activation energy of $MoSi_2$ oxidation with Kissinger method for $MoSi_2B$ sample

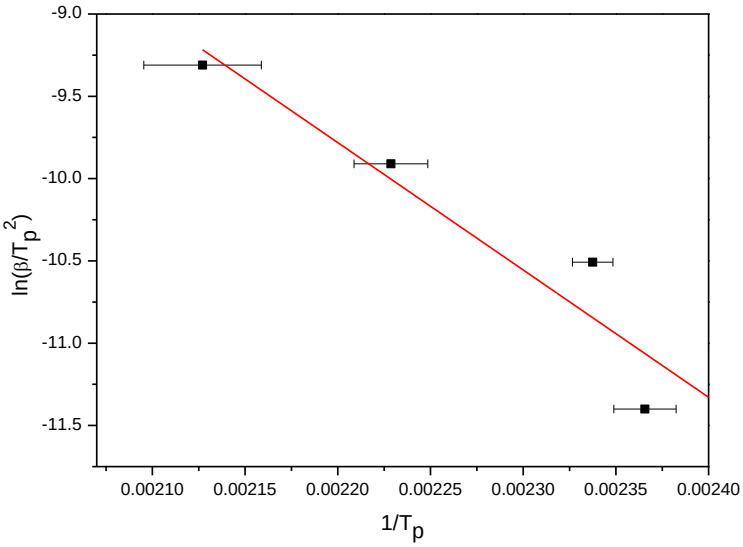

Figure 4.38: Determination of activation energy of $MoSi_2$ sample oxidation with Kissinger method

4.4.3 Thermal analysis on YSZ-$MoSi_2$ and YSZ-$MoSi_2B$ powder mixture

The same thermal analysis procedure as used for the oxidation of the $MoSi_2$ based powders is applied on the YSZ-$MoSi_2B$ powder mixture. The result of this analysis is shown in Figure 4.39. Both of the DTA and TG curves are different from $MoSi_2B$ sample. Exothermic peak of $MoSi_2$ oxidation cannot be clearly recognized from the DTA curve. Nevertheless, it is believed that the oxidation process occurs because the mass of the sample increases continuously until 1100 °C. There is no significant mass loss at 800 °C as $MoSi_2B$ sample, which indicates that the oxidation product remains in the sample during heating.

The YSZ powder is again proved to be stable during the annealing process, since no thermal event is observed from the DTA curve of YSZ. Comparison is made between the DTA curves

of YSZ-$MoSi_2B$ mixture, YSZ and $MoSi_2B$ powder; see Figure 4.40. Superimposing the curve of YSZ on the curve of $MoSi_2B$ cannot obtain the curve of the mixture below 1000 °C. Therefore, it can be concluded that the existence of the YSZ powder influences the oxidation behaviour of $MoSi_2B$.

The XRD result of YSZ-$MoSi_2B$ mixture after DTA measurement shows that $ZrSiO_4$ is formed during the experiment; see Figure 4.41. Since the reaction between ZrO_2 and SiO_2 is active above 1000 °C and the enthalpy of this reaction is negative [FACT oxide database/ FactSage] , an exothermic peak for zircon formation is expected in temperature region above 1000 °C. However, no such peak can be identified clearly in the DTA curve. Besides, no MoO_3 peak is found in XRD pattern, which suggests that MoO_3 may have escaped mainly during the cooling process.

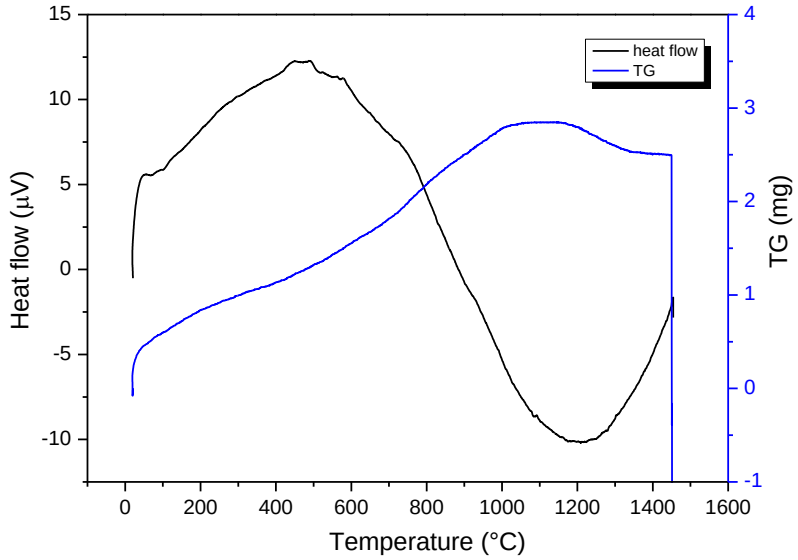

Figure 4.39: DTA and TG result on YSZ-$MoSi_2B$ powder mixture, heating rate 5 °C/min

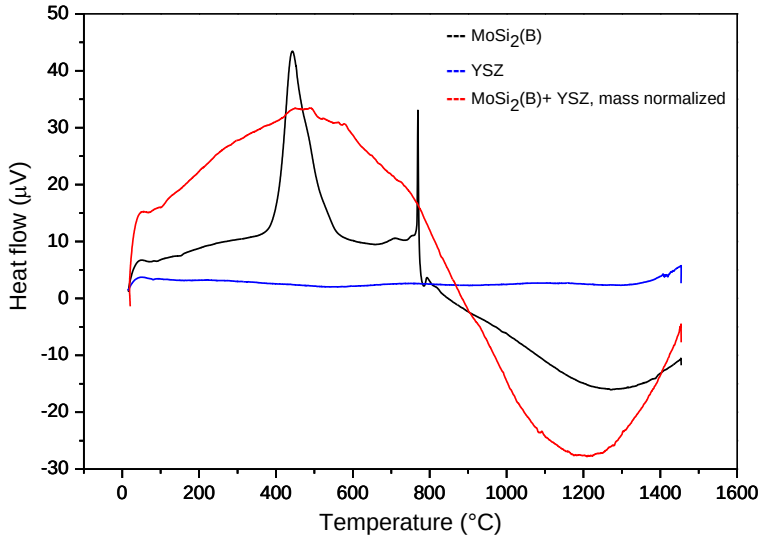

Figure 4.40: comparison between DTA curves of YSZ, $MoSi_2B$ powder and YSZ-$MoSi_2B$ mixture, heating rate 5 °C/min

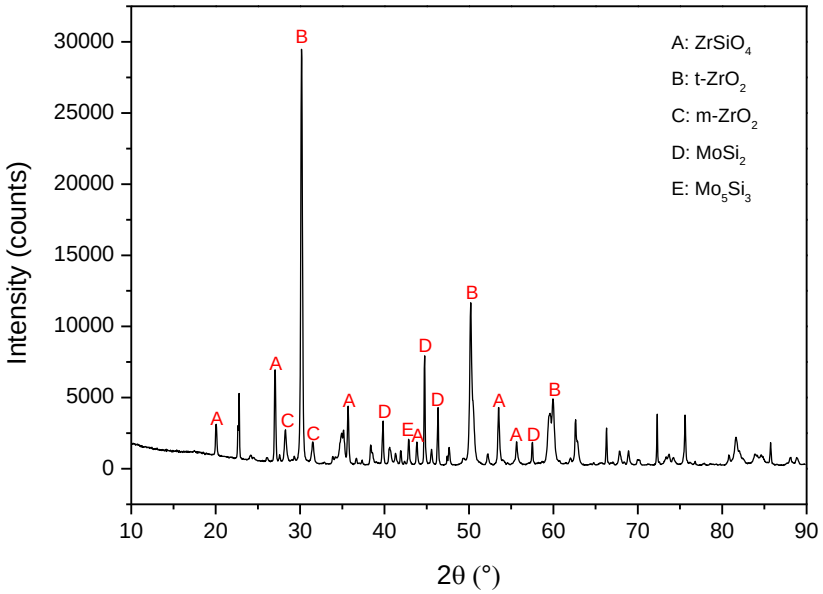

Figure 4.41: XRD pattern of YSZ-$MoSi_2$B mixture after DTA analysis

The result of the thermal analysis of YSZ-$MoSi_2$ mixture is shown in Figure 4.42. Similar to the system added with Boron, ZrO_2 also affects the oxidation behaviour of $MoSi_2$; see Figure 4.43. But the influence is less effective, since an exothermic peak can be identified between 400 to 500 °C. The mass of the sample keeps increasing during heating without any loss at 800 °C. Judged from the relative peak intensity of $ZrSiO_4$ phase in the XRD result, only a very small amount of $ZrSiO_4$ is formed, which indicates that the addition of Boron promotes the formation of $ZrSiO_4$. Still, the peak that corresponds to zircon formation can hardly be located in the DTA curve.

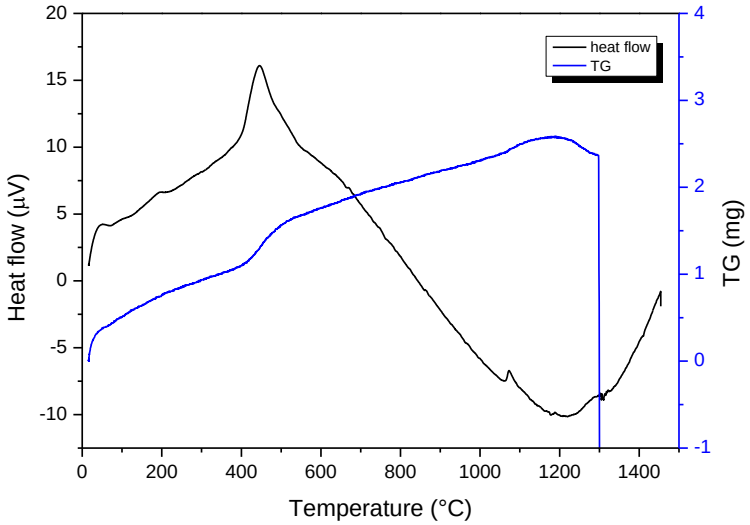

Figure 4.42: DTA and TG result on YSZ-$MoSi_2$ powder mixture, heating rate 5 °C/min

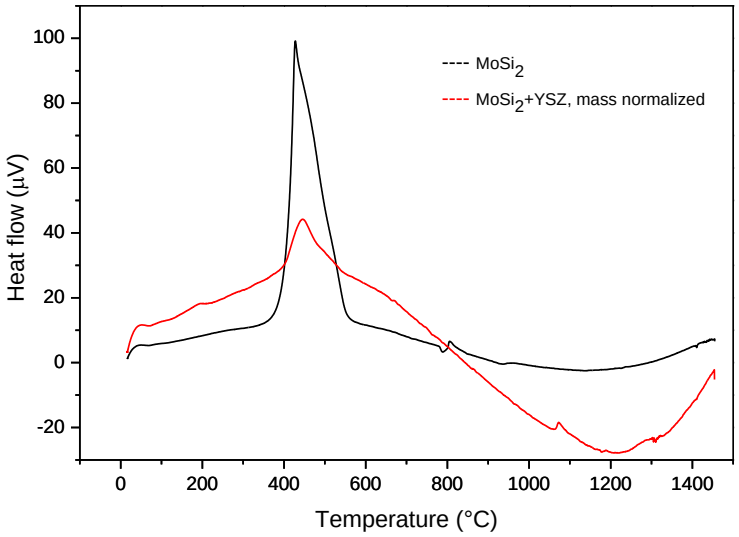

Figure 4.43: comparison between DTA curves of $MoSi_2$ powder and YSZ-$MoSi_2$ mixture, heating rate 5 °C/min

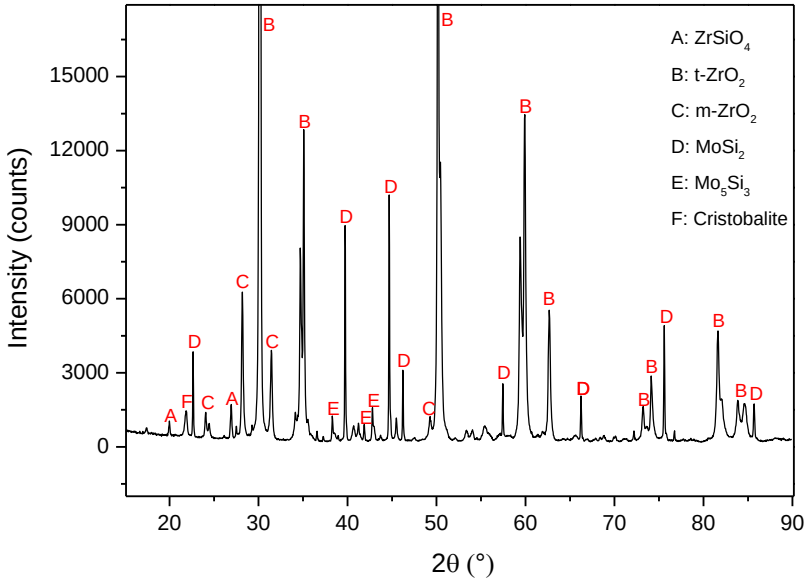

Figure 4.44: XRD pattern of YSZ-$MoSi_2$ mixture after DTA analysis

4.5 Discussion on the mechanism of ZrO_2-SiO_2 reaction

The kinetic data of ZrO_2 consumption upon reaction with SiO_2 (i.e. Figure 4.14 and Figure 4.15) can be used to determine the conversion function associated with the reaction forming zircon. All the conversion functions listed in Table 2.2 (see Chapter 2) were tried to fit the experiment results. For the YSZ-$MoSi_2$B sample annealed at 1200 °C in air, the change in the conversion fraction α of ZrO_2 during first four hours can be represented by the conversion function of the volume contraction model (R3), as shown in Figure 4.45. The good linearity of the first five data points proves that the mechanism of the reaction is the same during first 2 hours of annealing (e.g. activation energy and frequency factor). The deviation of the data points at 3 and 4 hours annealing from the linear fit may be due to the relative large error in the data. The reaction mechanism changes after annealing for 4 hours, since the data points after 4 hours cannot be fitted with the R3 function. The fitting of the data points of YSZ-$MoSi_2$ sample to R3 function starts from annealing time of 0.5 hours (see Figure 4.46),

because before that the oxidation rate of $MoSi_2$ limits the reaction between ZrO_2 and SiO_2. The relative lower speed of wetting by amorphous SiO_2 when Boron is absent may also influence the linearity of the data fitting result of YSZ-$MoSi_2$ sample.

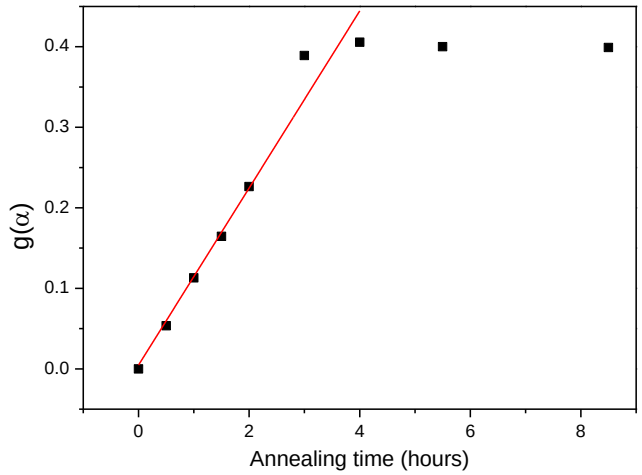

Figure 4.45: fitting of conversion function R3 to the experiment results of YSZ-$MoSi_2B$ annealed at 1200 ℃

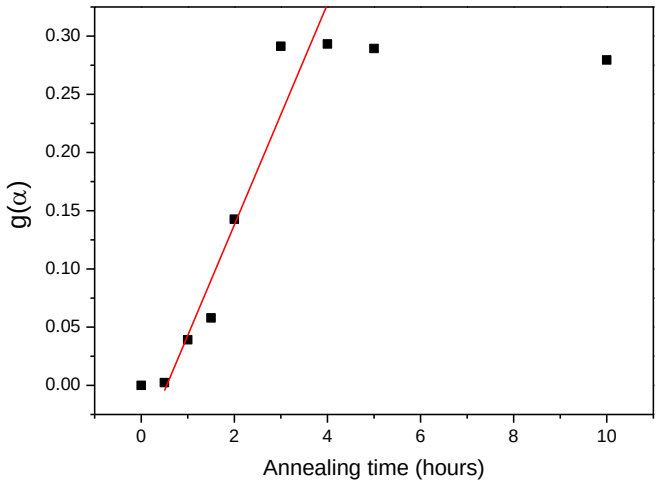

Figure 4.46: fitting of conversion function R3 to the experiment results of YSZ-$MoSi_2$ annealed at 1200 ℃

The SEM images of the microstructure of the YSZ-$MoSi_2B$ and YSZ-$MoSi_2$ tablets after annealing for 2 hours further substantiate the volume contraction model of the YSZ-SiO_2 reaction. As shown in Figure 4.47, zircon is formed at the surface of ZrO_2 particles and the diameter of remnant ZrO_2 particles shrinks after annealing.

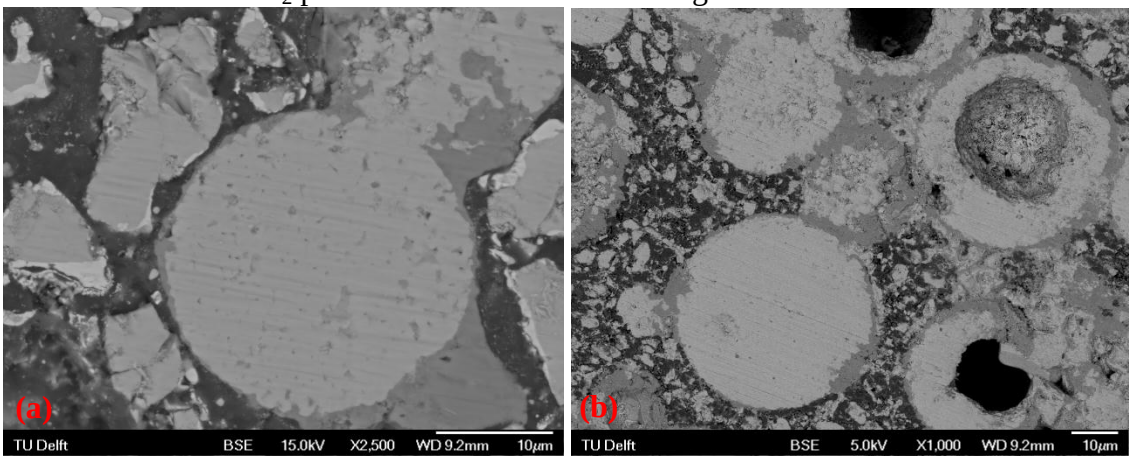

Figure 4.47: SEM image of tablets annealed at 1200 °C for 2 hours, (a) YSZ-$MoSi_2B$; (b) YSZ-$MoSi_2$

It is worth noting that the kinetics of solid-state reaction mainly depends on the rate of two reaction processes, namely the chemical reaction between reactants and the diffusion of the reacting species. The volume contraction model is derived on the basic assumption that the chemical reaction is the rate-determining step and diffusion of reactants is fast enough to be neglected. The decrease in the consumption rate of ZrO_2 with time is only due to the decrease in the surface area of ZrO_2 particles as the reaction proceeds.

As proposed by Eppler [20] and Veytizou [17], for the reaction between ZrO_2 and SiO_2, Si^{4+} is the cation diffusing species instead of Zr^{4+}. The SEM images of the microstructure after annealing in this study (e.g. Figure 4.16 and Figure 4.17) can qualitatively confirm their theory. The curvature of the interface between SiO_2 and $ZrSiO_4$ is similar to the curvature of the original ZrO_2 particles. If Zr^{4+} is the diffusing species and diffuses outwards into the SiO_2, the $ZrSiO_4$ will be formed inside the original SiO_2 area and the depletion of Zr element will generate Zr^{4+} vacancies at the interface between ZrO_2 and SiO_2. Such Zr^{4+} vacancies will diffuse to the inner area of ZrO_2 particles and finally coalesce to form a number of pores. However, such pores are not observed inside the remnant ZrO_2 phase.

The reaction model given by Veytizou et al. [17] is adopted to describe the mechanism of zircon formation in the YSZ-$MoSi_2$ (with and without Boron) sample. Oxygen molecules first enter the YSZ-$MoSi_2$ tablet through the porosity and oxidize the $MoSi_2$ particles. The SiO_2 formed is amorphous and it can fill the empty space in the sample and lead to a high contact area with ZrO_2 due to the volume expansion after oxidation. The SiO_2 dissociates into Si^{4+} interstitial ions and Si vacancies. The difference in the concentration of Si^{4+} ions between SiO_2 and YSZ is the driving force for the diffusion of Si^{4+} into YSZ. Since the lattice site in YSZ is not fully occupied due to oxygen vacancies, the Si^{4+} ions can partly dissolve in the tetragonal ZrO_2. Simultaneously, the concentration difference in the oxygen vacancy between YSZ and SiO_2 results in the diffusion of oxygen vacancies into SiO_2. $ZrSiO_4$ is formed at the interface between YSZ and SiO_2 and separates the two reactants. To continue the reaction, the diffusing species, namely Si^{4+} ions and O^{2-} vacancies, need to transport across the $ZrSiO_4$ layer. Therefore, a gradient in Si and O concentration as well as the overstochiometry in $ZrSiO_4$ layer are expected. Based on the result of volume contraction model fitting, the diffusion of species across $ZrSiO_4$ layer is relatively fast compared with the rate of chemical reaction between SiO_2 and ZrO_2.

EPMA was applied to the YSZ-$MoSi_2$ sample annealed for 15 hours at 1200 °C. The region at which a line scan is performed from the ZrO_2 area across the $ZrSiO_4$ layer and into SiO_2 is displayed in Figure 4.48a. The normalized intensity of the characteristic X-ray signal that corresponds with Zr and Si is plotted versus the distance from the starting point of the scan, as shown in Figure 4.48b. A concentration gradient of Si can be observed at the interface between $ZrSiO_4$ and ZrO_2. Such concentration profile is not related to the resolution of experimental techniques. This can be supported by an estimation of the volume of the electron beam-sample interaction. The electron beam radius is over-estimated as 100 nm for an electron beam current (20 nA) used in the EPMA experiment [32]. Using the software "Casino" with the same parameters in the EPMA test (e.g. accelerate voltage 5 kV, beam radius 100 nm), the distribution of the energy of the scattered incident electrons in the sample can be simulated; see Figure 4.49. It is estimated that for both ZrO_2 and $ZrSiO_4$, the diameter of the boundary at which the primary electrons lose 95% of energy after scattering in sample is about 0.3 μm. It is worth noting that the real value of the resolution in this EPMA experiment is smaller than 0.3 μm, because only those primary electrons with energy higher than the binding energy of electrons in the sample (i.e. Zr L shell and Si K shell) after

scattering are capable of generating characteristic X-rays. Moreover, the real electron beam radius is lower than 100 nm and the diameter of the interaction volume decreases with electron beam radius. The spacing between two spots along the scanning line as shown in Figure 4.48b is 0.25 μm. Therefore, it can be concluded that Figure 4.48b represents the element concentration profile in the ZrO_2 and $ZrSiO_4$ region.

The interface region between ZrO_2 and $ZrSiO_4$ is about 1.5 μm. The concentration gradient of Si at ZrO_2-$ZrSiO_4$ interface indicates the diffusion of Si from $ZrSiO_4$ into ZrO_2 during the reaction process. When the solubility limit for Si in ZrO_2 is reached, $ZrSiO_4$ can be formed and the interface moves into ZrO_2. A gradient of Si in the $ZrSiO_4$ layer can hardly be observed. However, it is anticipated that a chemical potential gradient of Si^{4+} ions exists and drives the diffusion of Si. A concentration gradient of Zr is also observed at the ZrO_2-$ZrSiO_4$ interface. However, it is expected that the flux of Zr is small compared with Si, because the diffusion coefficient of Zr in $ZrSiO_4$ is lower than that of Si [33] due to the high formation energy of Zr vacancies and interstitials [34].

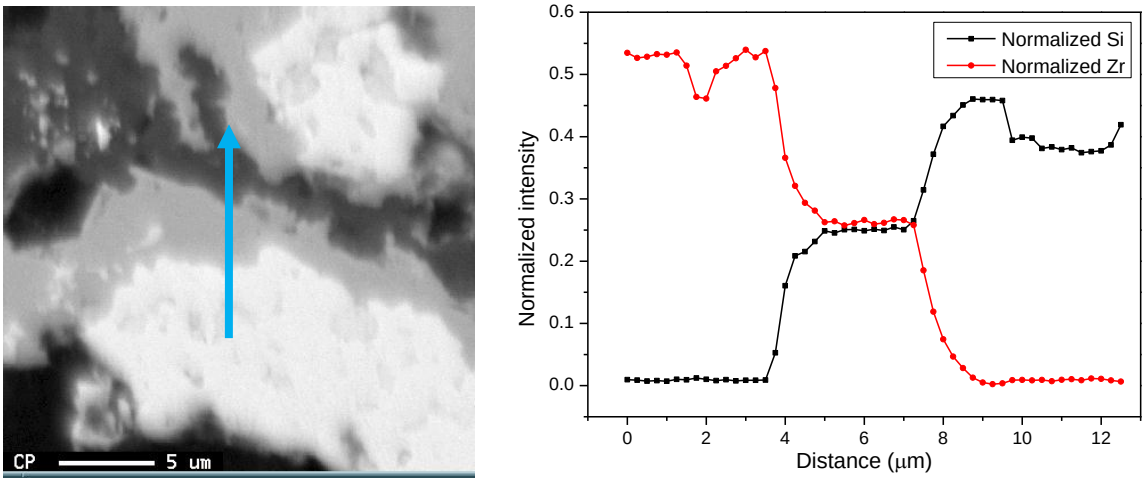

(a) (b)

Figure 4.48: Concentration profile of Si and Zr along the arrow direction, measured by EPMA

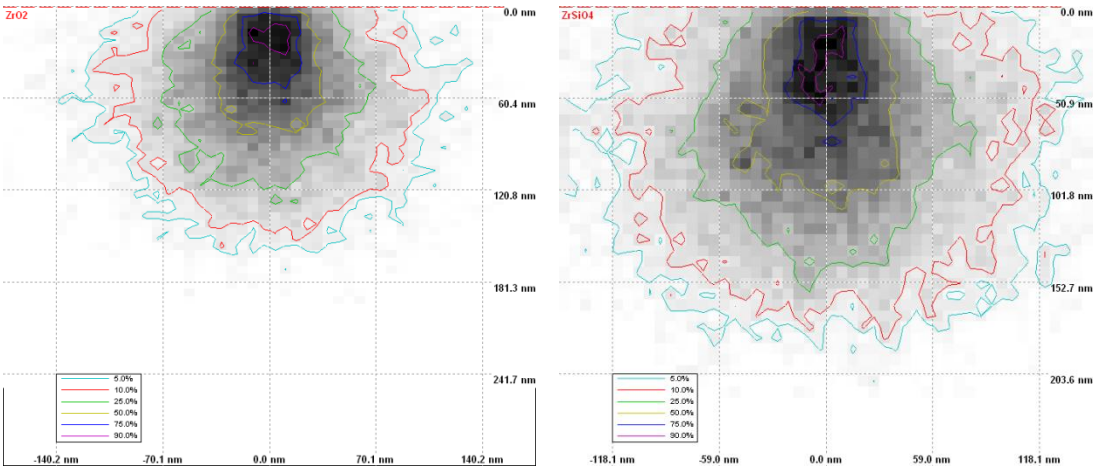

Figure 4.49: Energy distribution of incident electrons in ZrO_2 and $ZrSiO_4$ below the sample surface (XZ plane)

During the XRD analysis on the quantification of ZrO_2 amount in the sample (cf. Section 3.3.2), it is observed that the XRD peaks of ZrO_2 are broadened after annealing, see Figure 4.50. Such peak broadening is not caused by the change in YSZ properties due to annealing. This is supported by a comparison experiment in which the same XRD peaks of YSZ powder are compared before and after 4 hours of annealing; see Figure 4.51. No peak broadening

effect can be observed in YSZ powder after annealing, which indicates that there is no significant change in the structure of YSZ powder after annealing. Therefore, the main reason that causes the peak broadening is the reaction between ZrO_2 and SiO_2. Generally, small domain size and high concentration of dislocation makes XRD peaks broaden. However, annealing increases the domain size (energy of material tends to be lower by eliminating defects such as grain boundaries), and XRD peaks will become sharper after annealing. Moreover, usually ionic compounds are not expected to contain high density of dislocations [35]. Therefore, it is suggested that the peak broadening results from the ZrO_2 lattice distortion caused by the dissolution of Si element. Moreover, the volume effect of zircon formation (cf. Section 2.3) exerts force on the remnant ZrO_2, since the unreacted ZrO_2 is connected to $ZrSiO_4$ without any delamination found in SEM images. Such force is on a microscopic scale and may also lead to broadening of ZrO_2 peaks.

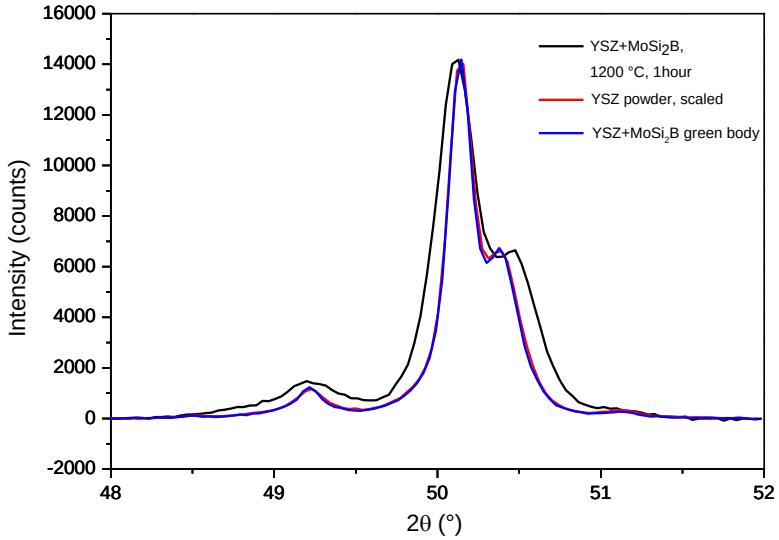

Figure 4.50: Comparison of XRD peaks of ZrO_2 between green body, annealed tablet and YSZ raw powder

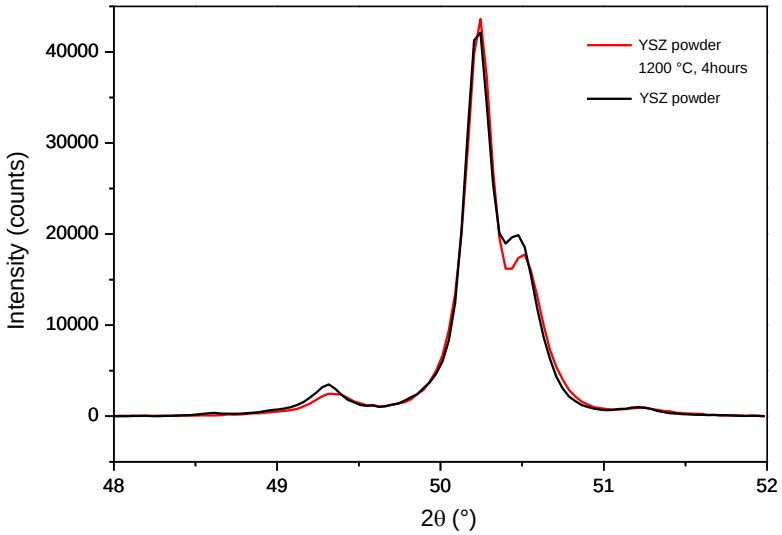

Figure 4.51: Comparison of XRD peaks of YSZ raw powder before and after annealing

The effect of Boron on the kinetics of zircon formation as well as the experiment results from YSZ-SiO_2 powder mixture clearly shows that the crystallinity of SiO_2 strongly affects the reaction between ZrO_2 and SiO_2. It is anticipated that the enthalpy for the formation of Frenkel defect in amorphous SiO_2 is much lower than that in crystalline SiO_2. The concentration of Frenkel defects can be expressed by [36]:

$$\frac{n}{N} = \exp(-\frac{\Delta G}{2kT}) \approx \exp(-\frac{\Delta H}{2kT})$$

, where *n/N* is fractional concentration, ΔG and ΔH are the change in Gibbs free energy and enthalpy respectively. Therefore, the concentration of Si^{4+} interstitial ions at the SiO_2-$ZrSiO_4$ interface is much higher when SiO_2 is in amorphous state. The higher gradient of Si^{4+} concentration across the two reactants, namely ZrO_2 and SiO_2, results in a high flux of Si ions into ZrO_2, which facilitates the reaction between SiO_2 and ZrO_2.

5 Conclusions

Crack healing in Yttria Stabilized Zirconia (YSZ) can be realized by reaction between amorphous silica (SiO_2) and zirconia (ZrO_2) at high temperatures forming stable zircon ($ZrSiO_4$). However, ZrO_2 does not react with crystalline SiO_2. Hence, zircon cannot be formed directly from a mixture of YSZ and SiO_2 powder. But, if instead of SiO_2 powder $MoSi_2$ (with and without Boron) is used, then upon high temperature oxidation amorphous SiO_2 is formed and the reaction with YSZ forming $ZrSiO_4$ proceeds.

The $MoSi_2$ is first oxidized resulting into MoO_3 and amorphous SiO_2. The MoO_3 is volatile at high temperature and fully escapes from the powder mixture. The amorphous SiO_2, due to oxidation of $MoSi_2$, is capable of filling the small gaps between the YSZ particles. The reaction between YSZ and SiO_2 is ceased after about 4 and 15 hours of annealing at 1200 and 1100 °C, respectively. At both annealing temperatures, the reactants are not fully consumed and the amount of remnant YSZ decreases with temperature.

The addition of Boron to $MoSi_2$ promotes the formation of amorphous SiO_2 and postpones the crystallization of amorphous SiO_2, and thus facilitates the formation of $ZrSiO_4$. The activation energy for the oxidation of $MoSi_2$ with boron is similar to that of $MoSi_2$ at temperatures ranging from 400 to 600 °C, viz. 75^{+8}_{-10} and 64^{+22}_{-14} kJ/mol, respectively.

The kinetics of ZrO_2 consumption and $ZrSiO_4$ formation can be represented by the conversion function of geometrical volume contraction model and first-order reaction model, respectively. This suggests that the kinetics of the crack healing reaction depends on the rate of chemical reaction between ZrO_2 and SiO_2 instead of the diffusion of reactant species. The initial rate of $ZrSiO_4$ formation in the YSZ-$MoSi_2$ powder mixture equals 0.0015 and 0.00037 mol/h at 1200 and 1100 °C, respectively. The addition of Boron increases the reaction rate, viz. 0.0014 and 0.00081 mol/h at 1200 and 1100 °C, respectively.

6 Recommendations

6.1 Isothermal kinetics

In order to quantify the measured X-ray intensities in terms of composition, an XRD measurement with same parameters should be applied with pure zircon crystal (without texture). Data on the evolution of the net area of zircon peak with time for the YSZ-$MoSi_2B$ sample annealed at 1200 °C needs to be completed. The rate of zircon formation with higher accuracy is to be determined from its kinetic curve.

Since the isothermal kinetics of the zircon reaction in the YSZ-$MoSi_2B$ sample annealed at 1100 °C is rather fast, data on the transformation of ZrO_2 and the formation of $ZrSiO_4$ at the early stages are required to determine the reaction rates.

In view of the envisioned application, i.e. crack healing in YSZ TBC, the kinetics of zircon formation at temperatures below 1100 °C will be attractive. The TBC in stationary gas turbine engines often operate at such temperatures.

6.2 Thermal analysis

The activation energy of zircon formation from the reaction between ZrO_2 and SiO_2 may be determined using a mixture of fine YSZ-$MoSi_2$ (with and without Boron) powders. Then the contact area between the reactants will be larger, because the smaller size of the particles the more dense the powder mixture will be. In this case more $ZrSiO_4$ is expected to be formed during DTA and the associate heat effect may be large enough to be observed.

It is suggested to apply more than four heating rates to obtain an accurate result for the activation energy.

6.3 Mechanism of zircon formation from YSZ-$MoSi_2$ system

The mechanism of $ZrSiO_4$ formation from the YSZ-$MoSi_2$ mixture is not fully understood yet. The result of conversion function fitting (see Figure 4.45) shows that in the tablet of YSZ-$MoSi_2$ powder mixture the rate of zircon formation is mainly subject to the chemical reaction between YSZ and SiO_2 instead of the diffusion rate of reacting species. This theory needs to be further substantiated by new experiments. A two-layer structured sample is available now; see Figure 6.1a. YSZ is air-plasma sprayed on top of $MoSi_2$ layer. After annealing, it is expected that a layer of SiO_2 is formed first at the interface between $MoSi_2$ and YSZ. Then, layer of $ZrSiO_4$ can be formed at the interface between SiO_2 and YSZ, and the front of $ZrSiO_4$ layer will be moving into the YSZ as reaction proceeds; see Figure 6.1b. Therefore, it will be very interesting to investigate the change of the thickness of $ZrSiO_4$ layer with annealing time by observing the cross-section of sample with SEM. If the chemical reaction between ZrO_2 and SiO_2 is the rate-determining step, then thickness of $ZrSiO_4$ layer will increase linearly with time. If, however, the diffusion of reacting species (e.g. Si^{4+} ions or O vacancies) dominates the kinetics, a parabolic relation between thickness and annealing time is expected.

Also an accurate quantitative analysis of the concentration profile across the SiO_2, $ZrSiO_4$ and ZrO_2 layers, may help to resolve the mechanism of the zircon formation. The over stoichiometry in $ZrSiO_4$ layer, namely the deficiency of oxygen, may be determined with EPMA.

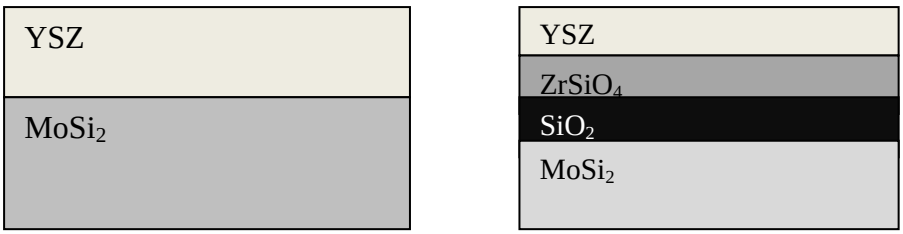

Figure 6.1: schematic picture of cross-section of the YSZ-$MoSi_2$ layer-structured sample before (a) and after (b) annealing

Further, it was observed that amorphous SiO_2 reacts with ZrO_2 faster than crystalline SiO_2; see Section 4.3. This difference in behaviour of amorphous and crystalline SiO_2 may be due to a higher concentration of Si^{4+} interstitial ions in amorphous than in crystalline SiO_2. To further prove this proposition, it is recommended that the enthalpy of the formation of Frenkel defect in amorphous SiO_2, quartz and cristoballite should be computed by ab initio method. It is anticipated that the computation result of enthalpy of Frenkel defect formation in amorphous SiO_2 is much lower than that in crystalline SiO_2.

Acknowledgement

I like to express my gratitude to my mentor Dr. Ir. Wim G. Sloof for his guidance throughout my thesis project. He is the most dedicated supervisor who not only shows great patience in answering my endless questions, but also inspired and offered me opportunities to challenge myself. He also guided me into the real world of materials science. Also I express my special thanks to Ruud Hendrikx, Niek van der Pers, Kees Kwakernaak, Hans Brouwer and Alexandra Carabat. Without their sincere help my thesis could never be completed. Finally, I like to thank all my friends and colleagues for both mental and technical support during the past 6 months. It was all you guys who made my thesis project the most joyful time in my Master program.

Reference:

[1] W. G. Sloof, "personal communications," ed, 2013.

[2] V.Kochubey and W.G.Sloof, "Self Healing Mechanism in Thermal Barrier coatings," in *ITSC proceedings*.

[3] E. C. Subbarao and K. V. G. K. Gokhale, "Thermal Expansion of Zircon," *Japanese Journal of Applied Physics*, vol. 7, 1968.

[4] G. V. G. Keith Robinson, P. H. Ribbe, "the structure of zircon: a comparison with garnet," *The American Mineralogist*, vol. Vol. 56, 1971.

[5] *Thermal barrier coatings*: Woodhead Publishing Limited, 2011.

[6] *Handbook of condensied matter and materials data*: Springer, 2005.

[7] H. G. Scott, "Phase relationships in the zirconia-yttria system," *Journal of Materials Science*, 1975.

[8] D. M. Cupid and H. J. Seifert, "Thermodynamic Calculations and Phase Stabilities in the Y-Si-C-O System," *Journal of Phase Equilibria and Diffusion*, vol. 28, pp. 90-100, 2007.

[9] Y. T. Zhu, M. Stan, S. D. Conzone, and D. P. Butt, "Thermal Oxidation Kinetics of MoSi2-Based Powders," *Journal of American Ceramic Society*, vol. 82, 1999.

[10] Y. T. Zhu, L. Shu, and D. P. Butt, "Kinetics and Products of Molybdenum Disilicide Powder Oxidation," *Journal of American Ceramic Society*, vol. 85, pp. 507-509, 2002.

[11] W. C. Butterman and W. R. Foster, "Zircon stability and the ZrO_2-SiO_2 phase diagram," *Am. Mineral.*, vol. 52, pp. 880-885, 1967.

[12] A. Kaiser, M. Lobert, and R. Telle, "Thermal stability of zircon (ZrSiO4)," *Journal of the European Ceramic Society*, vol. 28, pp. 2199-2211, 2008.

[13] C. Du, Q. Yuan, and Z. Yang, "Lowering the synthesis temperature of zircon powder by yttria addition," *Journal of Materials Science Letters*, 1999.

[14] T. Itoh, "Formation of polycrystalline zircon ($ZrSiO_4$) from amorphous silica and amorphous zirconia," 1992.

[15] T. Mori, H. Yamamura, H. Kobayashi, and T. Mitamura, "Formation mechanism of $ZrSiO_4$ powders," *Journal of Materials Science*, 1993.

[16] D. R. Spearing and J. Y. Huang, "Zircon synthesis via sintering of milled SiO_2 and ZrO_2," *Journal of American Ceramic Society*, 1998.

[17] J. F. Q. C. Veytizou, O. Valfort, G. Thomas, "zircon formation from amorphous silica and tetragonal zirconia: kinetic study and modelling," ed, 2001.

[18] E. C. S. S. V. Ramani, K. V. G. K. Gokhale, "Kinetics of zircon synthesis," 1969.

[19] R. A. E. Karen M. Trappen, "Reaction of zirconia with silica at the stoichiometry of zircon," *Journal of American Ceramic Society*, 1989.

[20] R. A. Eppler, "Mechanism of Formation of Zircon Stains," *Journal of the American Ceramic Society*, vol. 53, pp. 457-462, 1970.

[21] A. Khawam and D. R. Flanagan, "Solid-state kinetic models: basics and mathematical fundamentals," *J Phys Chem B*, vol. 110, pp. 17315-28, Sep 7 2006.

[22] H. E. Kissinger, "Variation of peak temperature with heating rate in differential thermal analysis," *Journal of research of the national bureau of standards*, vol. 57, 1956.

[23] T. Ozawa, "Estimation of activation energy by isoconversion methods," *Thermochimica Acta*, vol. 203, pp. 159-165, 1992.

[24] *Introduction to Thermal Analysis: Techniques and Applications*: Kluwer Academic Publishers, 2004.

[25] *Comprehensive chemical kinetics* vol. 22. Amsterdam: Elsevier Scientific Publishing Company, 1980.

[26] N. Birks, G. H. Meier, and F. S. Pettit, *Introduction to the high-temperature oxidation of metals*: Cambridge University Press, 2006.
[27] *The Mie Theory: Basics and Applications*: Springer Berlin Heidelberg, 2012.
[28] B. D. Cullity, *Elements of X-ray diffraction*, second ed.: Addison-Wesley Publishing Company, Inc., 1978.
[29] J. Goldstein, *Scanning electron microscopy and x-ray microanalysis*: Plenum, 1981.
[30] V. D. Scott, G. Love, and S. J. B. Reed, *Quantitative electron-probe microanalysis*, 2nd ed.: Ellis Horwood Limited, 1995.
[31] J. N. Reimers, J. E. Greedan, and M. Sato, "The crystal structure of the spin-glass pyrochlore, Y2Mo2O7," *Journal of Solid State Chemistry*, vol. 72, pp. 390-394, 2// 1988.
[32] "Instructions: JXA-8900R/RL WD/ED combined microanalyzers," ed.
[33] D. J. Cherniak, "Si diffusion in zircon," *Physics and Chemistry of Minerals*, vol. 35, pp. 179-187, 2008.
[34] R. E. Williford, W. J. Weber, R. Devanathan, and A. N. Cormack, "Native vacancy migrations in zircon," *Journal of Nuclear Materials*, vol. 273, pp. 164-170, 7// 1999.
[35] J. William D. Callister, *Materials Science and Engineering: An Introduction*, 7th ed.: John Wiley & Sons, Inc., 2007.
[36] Y.-M. Chiang, D. P. Birnie, and W. D. Kingery, *Physical Ceramics*: John Wiley & Sons, Inc., 1997.